Improving Constitutive Modelling of Soft Organic Clays With New Experimental Insight

Chao, Ching-Yu; Muraro, Stefano; Jommi, Cristina

DOI
10.1002/nag.70019

Publication date
2025

Document Version
Final published version

Published in
International Journal for Numerical and Analytical Methods in Geomechanics

International Journal for Numerical and Analytical Methods in Geomechanics

WILEY

RESEARCH ARTICLE OPEN ACCESS

Improving Constitutive Modelling of Soft Organic Clays With New Experimental Insight

Ching-Yu Chao[1,2] | Stefano Muraro[2] | Cristina Jommi[2,3]

[1]Department of Civil Engineering, National Cheng Kung University, Tainan, Taiwan | [2]Department of Geoscience and Engineering, Delft University of Technology, Delft, the Netherlands | [3]Department of Civil and Environmental Engineering, Politecnico di Milano, Milano, Italy

Correspondence: Cristina Jommi (C.Jommi@tudelft.nl)

Received: 8 April 2025 | **Revised:** 24 April 2025 | **Accepted:** 17 July 2025

Funding: The study was supported by NWO, the Dutch Organisation for Scientific Research, under the project 'SOFTTOP: Investigating heterogeneous soft top soils for wave propagation, cyclic degradation and liquefaction potential' with project number DEEP.NL.2018.006.

Keywords: constitutive modelling | extension stress paths | organic soils | pre-failure behaviour | triaxial tests

ABSTRACT

The engineering response of soft organic clays is controlled by anisotropy, stress history and the nature of organic matter. The behaviour of these soils has been investigated extensively over compression triaxial paths, and models are available to successfully reproduce available experimental observations. However, open questions remain about the response over stress paths other than compression. In this study, an organic diatomaceous clay from the Netherlands was subjected to an extensive experimental programme, which included monotonic and non-monotonic axis-symmetric stress paths in both compression and extension. The comprehensive study introduces a new dataset to support the development and calibration of constitutive approaches. The collected experimental data revealed some limitations in current elastic–plastic models, which were addressed by introducing greater flexibility in the shape of the yield function and enhancing previous rotational hardening rules. The new model, named JMC-clay, is assessed and validated over a variety of stress paths. The comparison between experimental data and numerical simulations demonstrates the ability of the model to accurately describe the pre-failure behaviour. The findings emphasise that the model performance is particularly sensitive to elastic–plastic compressibility more than any other parameter. It is suggested that the true bottleneck in the practical implementation of this class of anisotropic formulations is their accurate initialisation, rather than calibration.

1 | Introduction

Soft organic soils are commonly found as predominant natural geomaterials at the depths of interest for geotechnical engineering works in many deltaic areas around the world. With the increase in global population, structures and infrastructures construction on soft soils is becoming more and more extensive. Advancing the understanding of the mechanics of these soils is essential to optimise construction and maintenance techniques and ensure the long-term integrity of the engineering works. To this aim, reliable information is crucial for designing and assessing structures in compliance with both ultimate limit states and serviceability limit states, which require accurate predictions of the soil behaviour under both pre-failure and failure conditions.

Previous investigations have focused predominantly on compression stress paths in the meridian plane. These studies have revealed that organic clays are characterised by high compressibility, relatively high friction angles, stress-induced anisotropy, possible loss of structure and strain-rate dependency [1–9]. The findings have underpinned the development of various

constitutive models within the framework of elasto-plasticity, hypo-plasticity and bounding surface plasticity for simulation and application purposes [10–13]. Once a comprehensive and robust rate-independent model is established, extension to time/rate-dependent response and/or cyclic behaviour becomes relatively straightforward in the framework of elasto-visco-plasticity [14–17] or bounding surface visco-plasticity [12, 18, 19]. The success of this approach hinges on the ability of the parent rate-independent formulation to accurately reproduce soil behaviour over a variety of stress paths. Addressing the latter challenge is the focus of this research, in an attempt to improve modelling strategies for soft organic clays.

Focusing on elastic–plastic approaches, various models for soft clays have been proposed, following the work of Sekiguchi and Ohta [20] and Hashiguchi [21]. Most of these models address stress-induced plastic anisotropy through a rotational hardening rule applied to the yield function and plastic potential. Within this category, two models, S-CLAY1 [22] and SANICLAY [23], are particularly noteworthy. Both models expand upon the modified Cam clay (MCC) formulation [24] by incorporating a rotational hardening rule dependent on plastic strains. The primary difference between these two models lies in their use of associated (S-CLAY1) versus non-associated (SANICLAY) yield and plastic potential functions. The simpler associated formulation proves sufficiently accurate for a variety of applications. However, subtle features of the soil behaviour, such as the observed decrease in deviatoric stress before reaching the critical state on the wet side [6], cannot be captured by an associated formulation without additional model complexities. Some researchers attribute this behaviour to loss of structure, which has been modelled as a reduction of the elastic domain – softening – at increasing stress ratios [10, 25]. However, the experimental evidence can also be reproduced by adopting different shapes for the yield surface and plastic potential, leading to the development of a non-associated formulation [23, 26].

Despite extensive research on soft clays all over the world and significant experimental characterisation efforts within the Netherlands [27–30], advanced material modelling of Dutch soft clays lags behind, even at increasing demand for numerical modelling in the engineering practice. This research aims to address this gap with the twofold aim of: (i) expanding the database of experimental results for soft clays over various triaxial stress paths, including extension; and (ii) refining existing elastic–plastic models to better capture the pre-failure behaviour, which is crucial in the engineering application. Recognising that a non-associated formulation is better suited to most Dutch clays, SANICLAY [18] was selected as the starting platform. A new model, JMC-clay, is developed, which enhances the yield surface shape and rotational hardening rule to better fit the new comprehensive experimental evidence.

2 | Experimental Investigation

2.1 | Material Description

The material used in the experimental investigation was collected at the Leendert de Boerspolder in the Netherlands, where a full-scale test on a historical regional dyke was performed [31]. Samples were retrieved from the soft clay foundation layer using a 106 mm piston sampler at two locations as follows: between 6.1 and 7.3 m below the ground surface underneath the crest of the dyke, and between 3.9 and 4.4 m below the polder. To reduce bio-degradation, the material was stored in a climate-controlled room at 10 ± 1°C and 90% relative humidity. To avoid loss of organic matter, oven-drying for soil classification was performed at 60°C [32]. The specific gravity of the soil, Gs, was measured with a helium pycnometer [33] and the organic content, OC, was assessed by ignition at 440°C [34]. The material retrieved below the crest of the dyke is a clayey sandy silt with variable organic content ranging from 2.7% to 7.3%. The material from the polder side is silt with a higher clay fraction (38%) and an organic content of about 4%. The tested samples are divided into groups depending on their organic content and sampling location (groups (III) to (IX) below the crest of the dyke, group (X) from the polder side). Figure 1 reports the particle size distribution from wet-sieving and hydrometer analysis for the tested groups. Relevant index properties are summarised in Table 1.

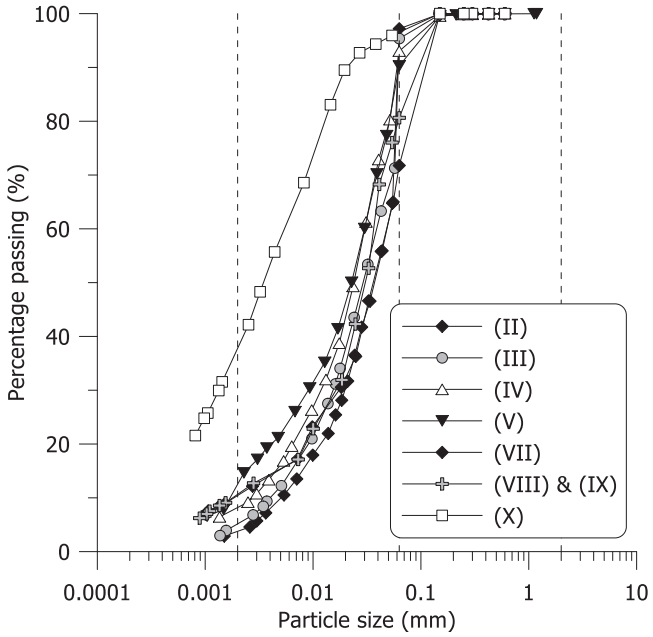

FIGURE 1 | Particle size distribution of the tested material.

TABLE 1 | Index properties of the material.

Index property	Value
Water content, w (%)	46–101
Plastic limit, w_p (%)	30–41
Liquid limit, w_l (%)	50–102
Plasticity index, I_p	20–61
% of particles < 0.002 mm	3–38
Organic content, OC (%)	2.7–7.3
Specific gravity, Gs	2.60–2.67

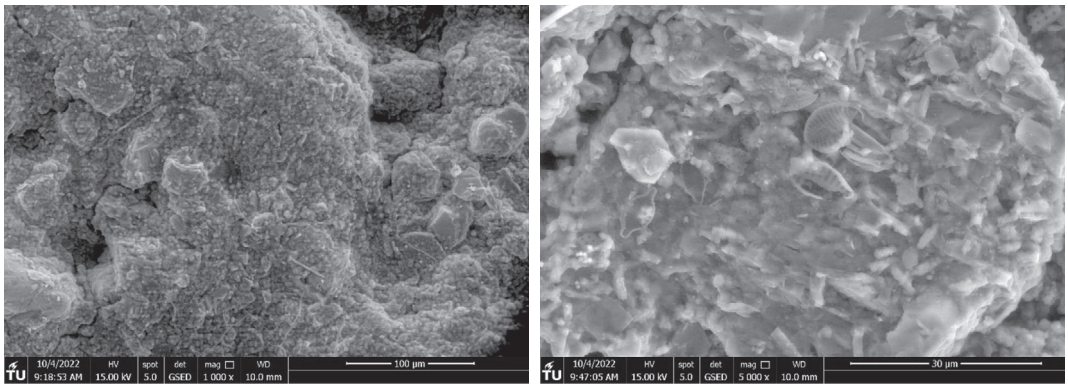

(a) (b)

FIGURE 2 | ESEM photomicrographs of the tested material (group VIII) at different magnification levels: (a) 1000× and (b) 5000×.

An impression of the fabric of the tested material is displayed in Figure 2 from ESEM photomicrographs. The sample was brought to the ESEM with an initial water content of about 47% which decreased during the test due to the chamber conditions. Temperature and relative humidity were not fully controlled during the tests, as the main focus of the ESEM was to assess the presence of diatom microfossils in the tested soil. The fabric is organised in aggregates with a characteristic size of the order of 100 µm (Figure 2a), where silt particles and diatoms microfossils are visible (Figure 2b).

2.2 | Testing Programme

To minimise sample disturbance, specimens with a nominal 38 mm diameter and 90 mm height were trimmed from the centre of the 106 mm piston sampler and tested in the triaxial apparatus. An initial height-to-diameter ratio of 2.5 was chosen to minimise end restraint effects [35, 36]. Table 2 collects an indication of the stress path followed on each sample, the initial void ratio, e_0; the organic content, OC; the maximum mean effective stress, $p'_{c,max}$ reached during the test and the mean effective stress at the start of the shear, p'_s. The triaxial system includes a submersible 1 kN load cell, back pressure and cell pressure volume controllers with an accuracy of ± 1 kPa on pressure and ± 200 mm^3 on volume (0.1% full-scale range). A suction cap was used to ensure perfect contact between the load cell and the top cap. All the drained tests were performed under stress control, ensuring a maximum excess pore pressure lower than 3 kPa.

Samples from groups (VI) and (IV) were brought to failure with standard TxCD tests or nearly constant p' tests (Figure 3a,b). Different loading histories (i.e., isotropic and K_0 compression, radial – $\eta = q/p'$ constant – compression and extension paths) and shearing constraints (i.e., TxCU, p' constant, q constant) were imposed on samples from groups (VII), (VIII) and (IX) as displayed in Figure 3c,d. K_0 stress-controlled compression tests were performed in the triaxial apparatus with volume change and axial displacement back measurement allowing for automatic adjustment to guarantee negligible radial strains. Multistage, loading–unloading, radial compression, constant p' and constant q stress paths were followed on the samples from the group (III) to better evaluate the non-monotonic pre-failure response (Figure 3e). Samples from the group (X) were compressed along different radial paths to specifically assess the evolution of anisotropy (Figure 3f).

3 | Results and Interpretation

The triaxial data are elaborated adopting the common triaxial stress–strain variables as follows: mean effective stress, p'; deviatoric stress, q; volumetric strain, ε_p and deviatoric strain, ε_q. Compressive stresses and strains are assumed positive. Natural strains [37] are adopted to avoid bias in the data interpretation caused by the large displacements attained by the samples [38].

3.1 | Compression Behaviour

The volumetric response upon isotropic and K_0 compression is displayed in Figure 4. A unique set of 1D and isotropic compression lines can be identified for each group, whose position depends on the initial void ratio as typically observed for silty soils (e.g., [39, 40]). The slope of the 1D virgin compression line, λ_{1D-VCL}, is slightly higher than the isotropic compression line, $\lambda_{ISO-NCL}$, as shown in Figure 4. An average ratio $\lambda_{1D-VCL}/\lambda_{ISO-NCL} = 1.14$ is found.

Dependence of the compression response on the organic content is also expected [41–43]. Figure 5 shows the influence of the organic content on the slope of the compression line for the tested soil, over the stress paths in Figure 3.

The experimental data show a consistent increase in λ from 0.1 to 0.35 with the organic content ranging from 2% to 7%, with the exception of samples from the group (X). Despite the similar organic content (e.g., VII and VIII), the higher compressibility of these samples, compared to other groups, might be attributed to their higher clay content (Figure 1). Additionally, inspection of ESEM photomicrographs reveals an abundance of large intact diatom microfossils in the matrix of samples from the group (X) (Figure 6) compared to a few and small broken diatoms inclusions in the group (VIII) (Figure 2b). The presence of large diatoms contributes to an increase in compressibility due to their hollow skeleton and trapped water in their intraskeletal pore space [44–49].

TABLE 2 | Initial state and type of stress path followed in the triaxial tests.

Tube	Sample ID	Test	OC (%)	Group	e_0 (−)	$p'_{c,max}$ (kPa)	p'_s (kPa)
B103-13	T1	Isotropic	6.4	III	1.97	149	26
	T2	K_0[a]	6.4		1.97	–	11
	T3	Mixed[b]	6.4		1.91	69	36
B103-13	T1	Mixed	6.0	IV	1.81	67	36
	T2	Mixed	6.0		1.71	68	36
B103-14	T1	p' constant	4.0	VI	1.26	14	14
	T2	TxCD	4.0		1.33	14	14
B103-14	T1	Isotropic	2.9	VII	1.51	–	7
	T2	K_0	2.9		1.40	–	7
	T3	Mixed	2.9		1.45	70	38
	T4	Mixed	2.9		1.47	70	38
B106-13	T1	Mixed	3.5	VIII	1.60	–	5
B106-13	T1	Mixed	2.7	IX	1.22	70	38
	T2	Mixed	2.7		1.24	69	39
	T3	K_0	2.7		1.21	–	6
B101-10	T4	K_0	2.2		1.17	–	7
B101-8	T1	Mixed	4.2	X	2.77	–	6
	T2	Mixed	4.5		2.74	–	6
	T3	Mixed	3.8		2.58	–	5
	T4	Mixed	3.5		2.61	–	7
	T5	Mixed	4.6		2.76	–	5
	T6	Mixed	3.7		2.60	–	6
	T7	K_0	3.4		2.28	–	6
	T8	Isotropic	3.2		2.24	–	5
	T9	K_0	3.2		2.39	–	5

[a]K_0 triaxial compression at null lateral strain.

[b]Mixed: various combinations of stress paths at constant stress ratio, p' constant loading–unloading and q constant paths (see Figure 3 for the specific soil samples).

3.2 | Shear Behaviour

The response upon shearing is summarised in terms of stress ratio, $\eta = q/p'$, versus deviatoric strain for different groups of samples. For the sake of clarity, only the last portion of each stress path up to failure is plotted. A uniform deformation mode was observed during the pre-failure response. For samples sheared in triaxial compression, failure was attained with a ductile barrel failure model. In extension, the formation of a neck shape at the mid-height of the sample was observed. The data after neck formation were excluded to ensure the representativeness of the analyses.

The results in Figure 7 show an ultimate stress ratio $M_{g,c} = 1.42$ in triaxial compression different than that in triaxial extension, $M_{g,e} = 1.05$, corresponding to different friction angles $\varphi'_c = 35°$ and $\varphi'_e = 39.5°$, respectively. A unique critical state surface in the $p' - q - e$ space was not identified for the tested material, as silty samples carry the information of their initial void ratio [40]. Samples from the group (VI) tested at very low confining stresses, $p' < 25$ kPa, attained a peak stress ratio equal to 1.8 before tending asymptotically towards the ultimate stress ratio. Samples T2 and T3 from the group (III) showed a slightly higher ultimate stress ratio at large strains due to poor controllability when the samples approached failure under q-constant stress path (Figure 3e). Contrarily to organic fibrous soils, the absence of significant differences in the ultimate friction angle within the investigated organic content indicates a highly decomposed nature of the organic matter in the tested material.

The ultimate friction angle in triaxial compression $\varphi'_c = 35°$ gives a reasonably consistent estimate of the at-rest lateral earth pressure coefficient in normally consolidated conditions using Jaky's simplified relationship ($K_0 \cong 1 - \sin\varphi'_c = 0.43$) compared to the experimental values, K_0^{NC} (0.43–0.48), determined from sample T2 (III), T2 (VII), T3 (IX) and T7 (X). Figure 8a reports the trend of the lateral stress ratio, $K_l = \sigma'_r/\sigma'_a$, during the K_0 compression tests. For samples T3 (IX) and T4 (IX), the test included a K_0 loading and unloading path. Figure 8b reports the development of the lateral stress ratio versus the overconsolidation ratio, OCR,

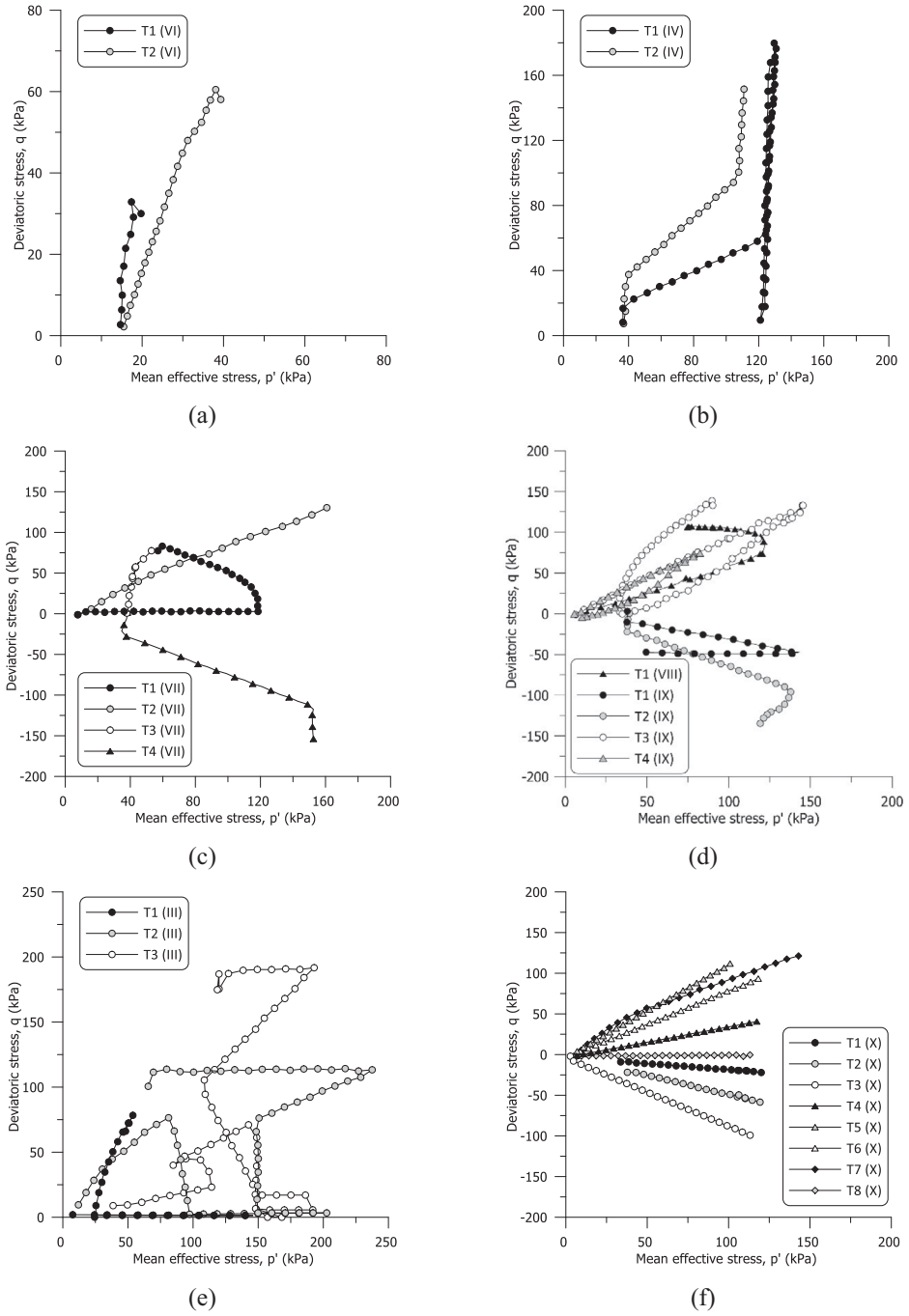

FIGURE 3 | Experimental stress paths followed in the triaxial tests for groups of samples: (a) (VI), (b) (IV), (c) (VII), (d) (VIII)–(IX), (e) (III) and (f) (X).

compared with the relationship [50]

$$\frac{K_0^{OC}}{K_0^{NC}} = OCR^m \tag{1}$$

where K_0^{OC} is the at-rest lateral earth pressure coefficient in over-consolidated conditions and OCR is the overconsolidation ratio in terms of axial effective stress. Figure 8b proposes a comparison between the experimental data and the commonly adopted value of $m = 0.5$ and $m = \sin\varphi'_c$ [51]. The experimental data seem to suggest $m = 0.42$ for the tested material.

Different responses upon K_0 compression among the tested samples can be observed in Figure 8a. Samples T2 (III), T7 (X) and T9(X) show a significant decrease in the lateral stress ratio at around $\sigma'_a \cong 50$ kPa, followed by a gradual increase towards the asymptotic value. This 'shoulder' shape of the lateral stress ratio has already been noticed by numerous authors (e.g., [52, 53]). Cotecchia and Chandler [54] suggested fabric changes associated with the transition between pre- and post-yielding domains as an explanation of this behaviour. Additional insight on K_0 compression response is provided in Figure 9, where the results are plotted in terms of void index [2], I_v, for both undisturbed and reconstituted samples of each group. The results seem to

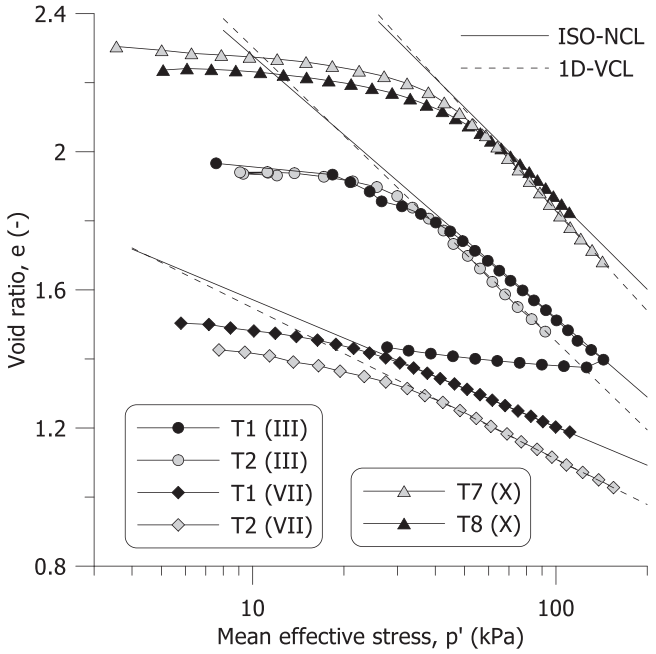

FIGURE 4 | Isotropic and K_0 compression paths for samples from groups (III), (VII) and (X).

suggest a more pronounced initial decrease in the lateral stress ratio, followed by an increase for those samples whose state lies well above the ICL (T2 (III), T7 (X), T9(X)). In contrast, samples T2 (VII), T3 (IX) and T4 (IX), which lie close to the ICL, show a monotonic gradual decrease in the lateral stress ratio.

3.3 | Yield Locus

The initial position and shape of the yield locus for the tested material were derived by exploiting the multiple stress paths in Figure 3. Various criteria were adopted to this aim [55, 56], and the points best matching all of them were eventually chosen (see Muraro and Jommi [57] for a detailed discussion). The experimental yield points in Figure 10 suggest an anisotropic yield locus, rotated on the p' axis.

To fit the experimental yield points, the expression proposed by McDowell and Hau [58] was chosen and extended to account for anisotropy:

$$f = 0 = (q - p'\alpha_f)^2 + \frac{(M_f{}^2 - \alpha_f{}^2)}{k_f - 1} p'^2 - \frac{(M_f{}^2 - \alpha_f{}^2)}{k_f - 1} p'_c{}^2 \left(\frac{p'}{p'_c}\right)^{\frac{2}{k_f}} \quad (2)$$

where α_f defines the inclination of the yield locus in the $p' - q$ space and p'_c is the pre-consolidation mean effective stress. The chosen surface allows enough flexibility in the shape through the two coefficients k_f and M_f. Standard shapes can be recovered, including the anisotropic version of the modified Cam clay model proposed by Dafalias [59] for $k_f = 2$. As displayed in Figure 10, the experimental yield points are nicely fitted by Equation (2) with $M_{f,c} = 0.99$, $M_{f,e} = 0.74$, $k_f = 1.25$ and $\alpha_f = 0.51$. The initial inclination of the yield locus was determined as described by Dafalias et al. [23], assuming $\kappa/\lambda = 1/9$ and $\nu = 0.2$.

Figure 10 also shows a comparison between the experimental plastic strain increment vectors computed along the different stress paths at the onset of yielding and the theoretical ones assuming normality condition with the yield locus in Equation (2). The volumetric and the deviatoric plastic strain increments, $\delta\varepsilon_p^p$ and $\delta\varepsilon_q^p$, have been derived from the total ones by computing the elastic strain increments, $\delta\varepsilon_p^e$ and $\delta\varepsilon_q^e$, with a hypo-elastic isotropic law with a constant Poisson's ratio, $\nu = 0.2$:

$$\delta\varepsilon_p^e = \frac{\delta p'}{K}; K = \frac{\upsilon p'}{\kappa} \quad (3)$$

$$\delta\varepsilon_q^e = \frac{\delta q}{3G}; G = \frac{3(1-2\nu)}{2(1+\nu)} K \quad (4)$$

where υ is the specific volume, K is the bulk stiffness, κ is the slope of the unloading–reloading compression line, G is the shear modulus, $\delta p'$ and δq are the increments in the mean effective stress and deviatoric stress, respectively. For each radial path, the value of κ has been determined from the experimental data. The comparison in Figure 10 suggests that the normality assumption does not hold for the tested material, as already highlighted by other authors on similar soils [60, 61]. It is worth remarking that the parameters $M_{f,c}$ and $M_{f,e}$ from Equation (2) are not related to the friction angle. These parameters are shape factors for the yield locus. The adoption of a non-associated flow rule with $M_f < M_g$ allows reproducing a decrease in the deviatoric stress before attaining the failure line during shearing in undrained compression, which is often observed in K_0 normally consolidated samples [23].

3.4 | Anisotropic Plastic Deformation Mechanism

Natural soft clays are expected to exhibit anisotropic response due to both the previous stress history (i.e., depositional conditions) and the subsequent loading [22]. The post-yielding plastic deformation response was analysed in terms of inclination β of the plastic strain increment vectors, where

$$\tan\beta = \frac{\delta\varepsilon_q^p}{\delta\varepsilon_p^p} \quad (5)$$

along stress paths at constant stress ratio.

Figure 11 shows a progressive reorientation of the plastic strain increment vectors along radial paths at constant stress ratio. The magnitude of the rotation depends on the previous stress history and loading direction. For the K_0 compression test on sample T3 (IX), the plastic strain increment vectors do not rotate as a result of the initial alignment of the fabric along the K_0 line.

The experimental evidence in Figure 11 justifies adopting an anisotropic stress-dilatancy rule (i.e., anisotropic plastic potential) such as the well-established expression proposed by Dafalias [59]

$$d = \frac{1}{\tan\beta} = \frac{M_g{}^2 - \eta^2}{2(\eta - \alpha_g)} \quad (6)$$

where d is the dilatancy, M_g is the critical stress ratio, and α_g is a non-dimensional anisotropic variable, which accounts for

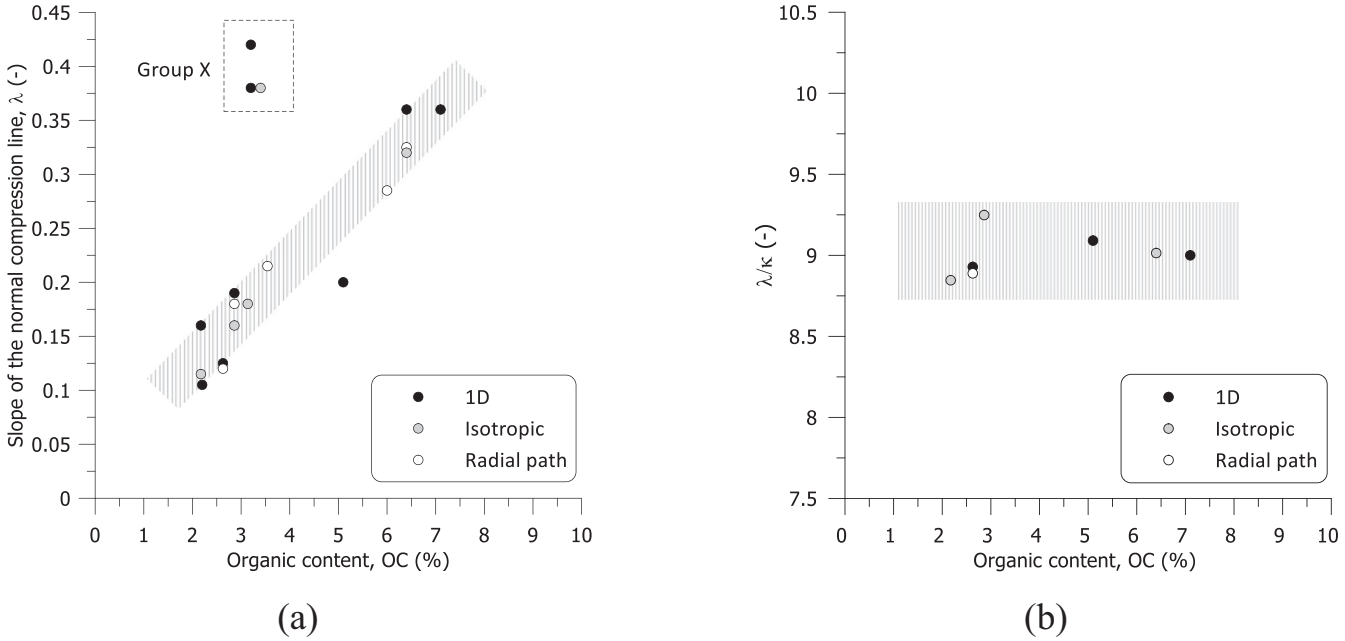

FIGURE 5 | Variation of (a) the slope of the compression line with the organic content, (b) the ratio between the slope of the compression line and the slope of the reloading line with the organic content.

FIGURE 6 | ESEM photomicrograph of the tested material from the group (X).

coupling of the deviatoric and volumetric plastic strain rates, and introduces the anisotropic response in the plastic deformation mechanism. By integrating Equation (6), the plastic potential reads:

$$g = \left(q - p'\alpha_g\right)^2 + \left(M_g{}^2 - \alpha_g{}^2\right) p' \left(p' - p'_g\right) \tag{7}$$

where p'_g is a dummy variable.

As shown in Figure 11, with enough straining along radial paths, the inclination of the plastic strain increment vectors reaches a fairly constant value. At this stage, Equation (6) allows deriving the asymptotic values of α_g called 'equilibrium or bounding' values, α_{gb}, for different radial paths [62]. To account for the different friction angles in triaxial compression and extension observed in Figure 7, it is suggested that the experimental data can be normalised with a critical stress ratio that depends on the Lode angle, $M(\theta)$. In Figure 12, the current experimental data normalised with $M_{g,c}$ for triaxial compression $\eta > 0$ and $M_{g,e}$ for triaxial extension $\eta < 0$ are compared with the two most used analytical expressions, namely the S-CLAY1 [22] and the SANICLAY [23]. The parameters of the reference analytical expressions were calculated based on the K_0 compression tests as described by Wheeler et al. [22] and Dafalias et al. [23]. As shown in Figure 12, both models fit reasonably well on the experimental data of the triaxial compression domain. However, the agreement is progressively lost in the extension domain, especially towards high stress ratios, $\eta/M_{g,e} < -0.5$.

To better fit the new experimental evidence in Figure 12, the expression proposed by Dafalias and Taiebat [62] is amended by weighing the asymptotic behaviour with a strictly positive power coefficient, y, and giving the de-amplification factor, (z in the original proposal), a dependency on the Lode angle as suggested by the experimental data.

For triaxial compression and extension, the proposal reads

$$\begin{aligned} \alpha_{gb} &= \frac{M_{g,c}}{z_c}\left[1 - \exp\left(-s\frac{|\eta|}{M_{g,c}}\right)\right]^y \text{ if } \eta \geq 0 \\ \alpha_{gb} &= -\frac{M_{g,e}}{z_e}\left[1 - \exp\left(-s\frac{|\eta|}{M_{g,e}}\right)\right]^y \text{ if } \eta < 0 \end{aligned} \tag{8}$$

where s is a positive model constant and z_c, z_e are the values of z over triaxial compression and triaxial extension, respectively. This choice implies that the model can attain different critical state lines in compression and extension paths, as already observed on different types of clays [63]. The experimental data for a wide range of stress ratios were fitted with the proposed equation with $y = 2$, $z_c = 1.6$, $z_e = 1.2$ and $s = 2$, as plotted in Figure 12.

It is worth mentioning that the results in Figure 12 are derived from experimental results of asymptotic plastic strain increment

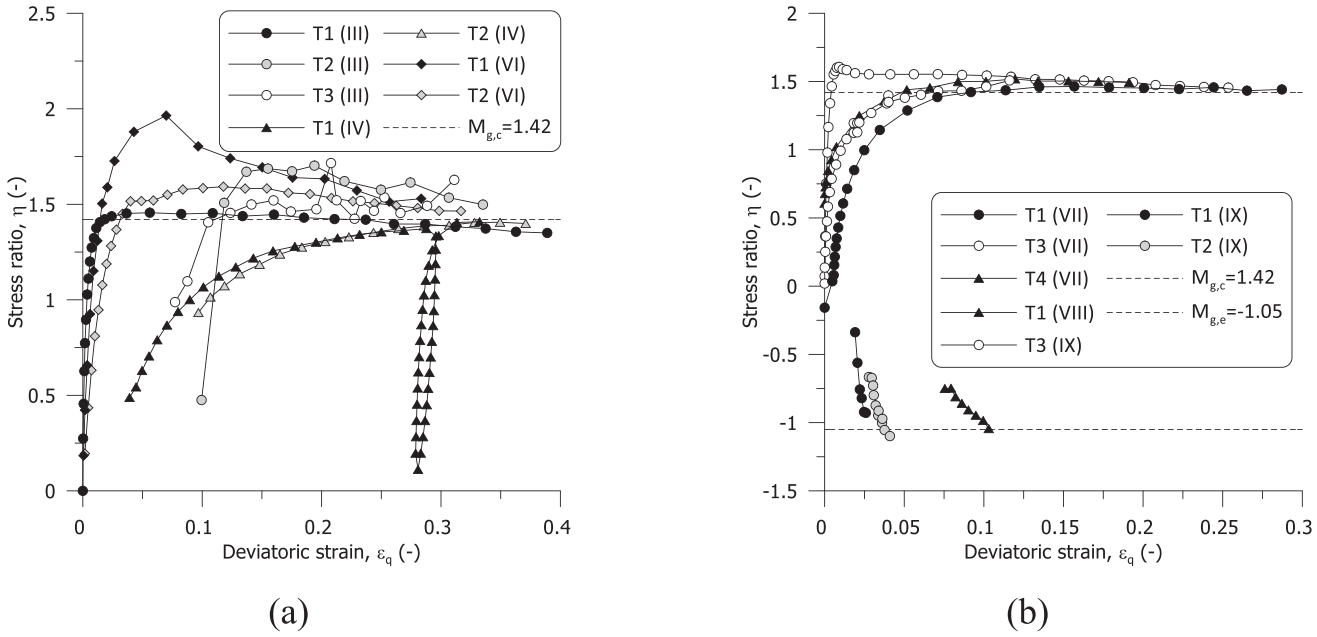

FIGURE 7 | Stress ratio versus deviatoric strain during the final shearing stage up to failure for samples from groups: (a) (III), (IV), (VI) and (b) (VII), (VIII), (IX).

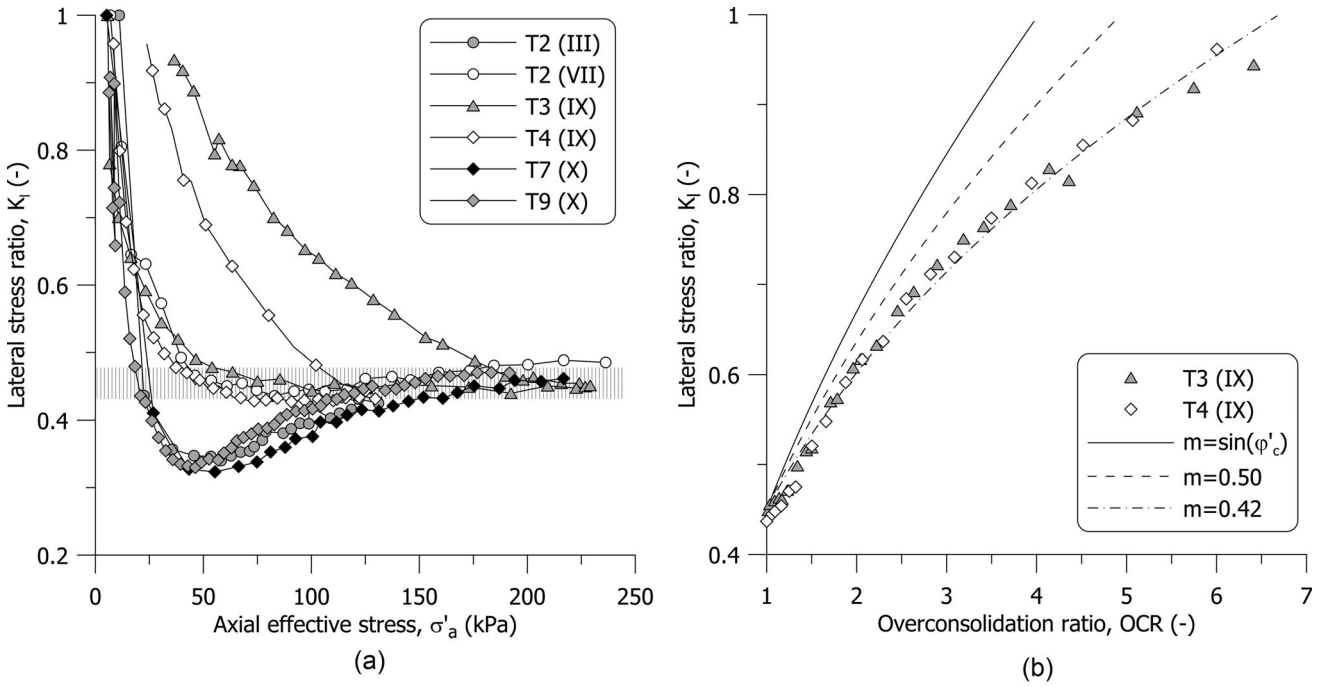

FIGURE 8 | Results from K_0 compression tests: (a) evolution of the lateral stress ratio and (b) change in K_0 with the overconsolidation ratio.

vectors after fixing the plastic deformation mechanism (i.e., the plastic potential in Equation 7). If the information in Figure 12 is also used to infer the evolution of anisotropy of the yield surface, Equation (8) can be adopted in the rotational hardening rule, assuming that $\alpha_f = \alpha_g = \alpha$ [18, 62, 64].

3.5 | Hardening Mechanism

Critical state models often assume that the current size of the yield surface is controlled solely by plastic volumetric strains, however, information on organic soils is still scarce. Muraro and Jommi [57] provided evidence that in highly organic peats the hardening mechanism is also ruled by deviatoric plastic strains, likely due to the rearrangement/realignment of the fibres contributing to the peat fabric. To discriminate between the two hypotheses for the tested material, the results of drained probe tests are analysed. Figure 13 reports the evolution of the normalised pre-consolidation pressure, $p'_{c,n}$, with the volumetric plastic strains, ε_p^p, computed along different radial paths. The normalised pre-consolidation pressure is calculated by dividing the current value by the one attained when the inclination of the

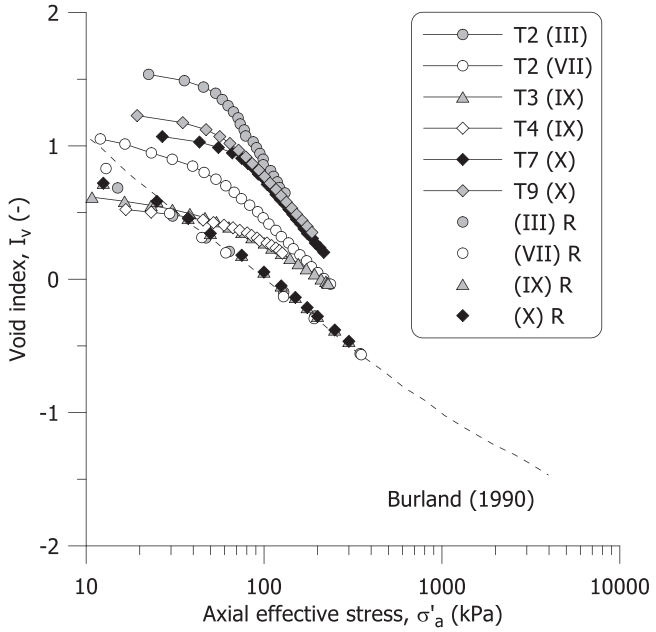

FIGURE 9 | Results from the K_0 compression tests in terms of void index.

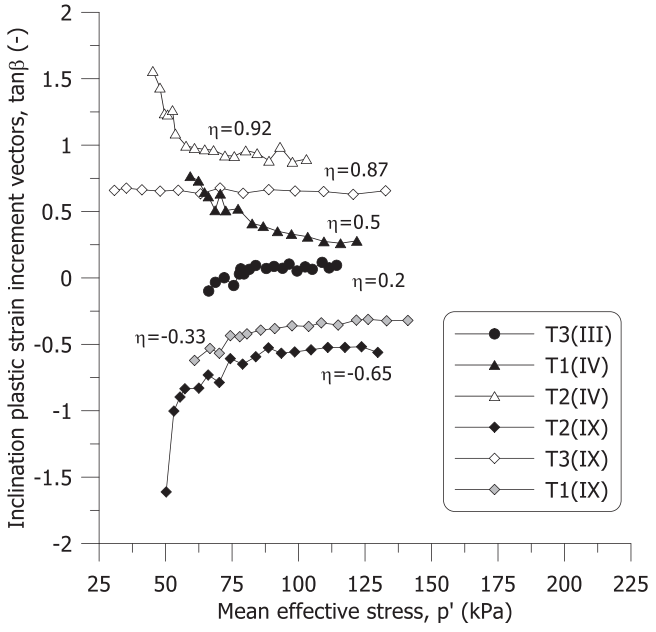

FIGURE 11 | Change in the inclination of the plastic strain increment vectors along radial paths.

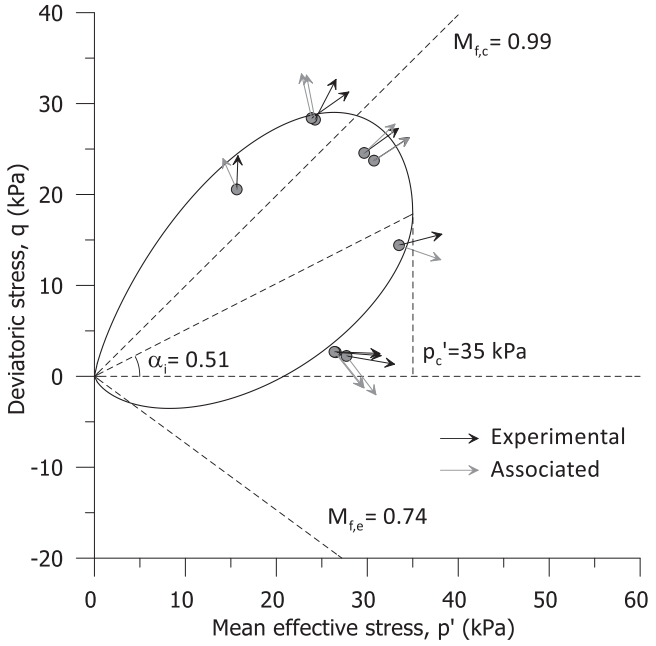

FIGURE 10 | Trace of the yield locus on the $p' - q$ space from the estimated yield points and corresponding plastic strain increment vectors.

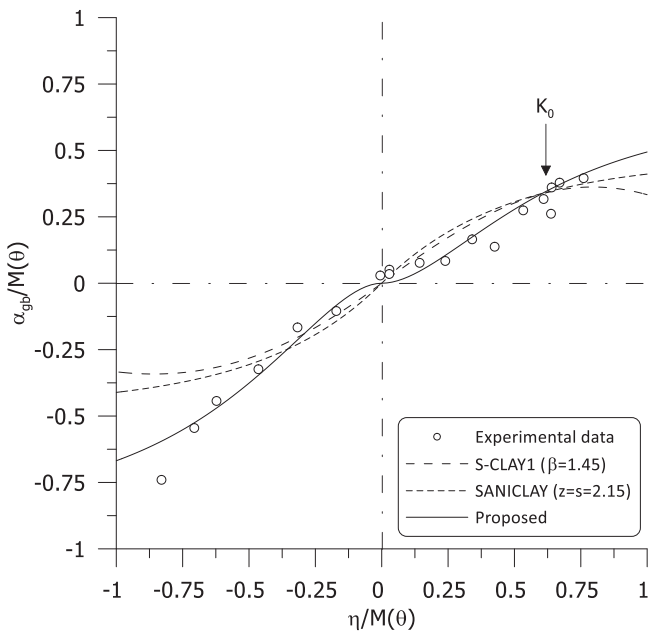

FIGURE 12 | Bounding values of α_{gb} for different radial paths.

yield locus, α, reaches the asymptotic value over the radial stress path. This choice allows isolating the change in the size of the yield locus from the change in its inclination.

The evidence in Figure 13 supports the assumption that the size of the yield locus for organic clays is ruled solely by plastic volumetric strains, as opposed to highly organic fibrous soils like peats. All the experimental data align well with the traditional volumetric hardening law [56]

$$\frac{\delta p'_c}{p'_c} = \frac{\upsilon}{\lambda - \kappa} \delta \varepsilon_p^p \tag{9}$$

A second hardening rule is needed to control the rotation rate of the yield locus produced by plastic straining. As anticipated, adhering to a common choice (e.g., [18, 64]), the rotational rule derived for the plastic potential (Equation 8) is also used for the yield locus. The suggestion by Dafalias and Taiebat [62] is chosen for the rotation rate, $\delta\alpha = \delta\alpha_g = \delta\alpha_f$, with

$$\delta\alpha = \langle L \rangle c p_{atm} \frac{p'}{p'_c} \left(\alpha_{gb} - \alpha\right) \tag{10}$$

where the plastic multiplier, L, is enclosed in the Macauley brackets <> to track plastic loading (i.e., $L > 0$ and $\langle L \rangle = L$) and elastic unloading (i.e., $L \leq 0$ and $\langle L \rangle = 0$), p_{atm} is the

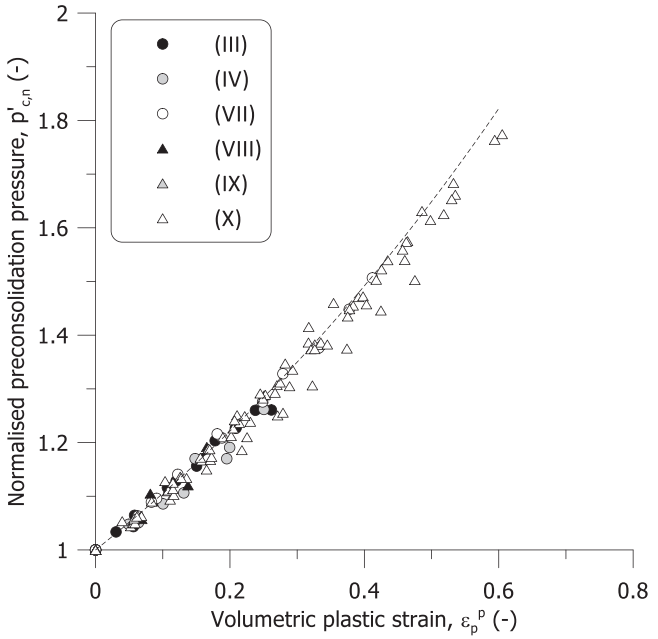

FIGURE 13 | Evolution of the normalised pre-consolidation mean effective stress with volumetric plastic strain for different radial stress paths.

atmospheric pressure, p'_c is the preconsolidation pressure, c is a model parameter controlling the rate of the evolution of α, and α_{gb} is the bounding value of α attained along the reference constant stress ratio path (Equation 8 and Figure 12).

4 | Numerical Calibration, Predictions and Validation

The elastic–plastic model built on the previous experimental findings is named JMC-clay. Its capabilities are discussed by simulating the laboratory tests with a single Gauss point scheme. To highlight the benefits of the JMC model over previous formulations, for a few specific tests a simulation with SANICLAY model [62], which served as a reference model for this work, is included. Where the simulation with SANICLAY is not reported, the two models perform in an almost identical way.

4.1 | Model Calibration Procedure

The model requires calibration of 12 parameters, which can be determined as follows:

- κ^*, λ^* are calibrated on loading and unloading–reloading paths such as isotropic or K_0; it is worth reminding that in the JMC model, κ^* and λ^* are defined on the $\ln(v) - \ln(p')$,
- ν is estimated by analysing the slope of the initial part of the K_0 unloading path on the $p' - q$ space, assumed to be elastic;
- $M_{g,c}$, $M_{g,e}$ are determined from triaxial compression and extension tests;

TABLE 3 | Model parameters adopted in the JMC simulations.

$M_{g,c}$	$M_{g,e}/M_{g,c}$	ν	c	z_c	z_e	s	y	$M_{f,c}$	k_f
1.42	0.74	0.2	50	1.6	1.2	2.2	2	0.99	1.25

TABLE 4 | Model parameters adopted in the SANICLAY simulations.

$M_{g,c}$	$M_{g,e}/M_{g,c}$	ν	c	z	s	$M_{f,c}$	k_f
1.42	0.74	0.2	50	2.15	2.15	0.99	2.0

TABLE 5 | Calibrated values of λ^* for different groups of samples depending on their organic content.

Parameter	(III)–(IV)	(VII)	(VIII)	(IX)	(X)
λ^*	0.137	0.085	0.095	0.065	0.140

- z_c, z_e, s and y are defined by fitting Equation (8) on at least three triaxial tests: K_0 compression and two radial paths at a constant stress ratio, one in compression and one in extension; if no data are available on the extension side, z_e can be obtained assuming $z_e/z_c = M_{g,e}/M_{g,c}$;
- $M_{f,c}$, $M_{f,e}$ and k_f are determined from yield points along drained stress probe paths; if no yielding data are available on the extension side $M_{f,e}$ can be obtained assuming $M_{f,e}/M_{f,c} = M_{g,e}/M_{g,c}$.
- The parameter c, which governs the rate of evolution of α, is calibrated by conducting trial runs, having all other constants calibrated in advance, to simulate the re-alignment of plastic strain increment vectors along a radial path. Suitable tests for this calibration are those that cause significant rotation of the plastic potential. A K_0 loading–unloading test followed by isotropic compression is recommended to maximise the number of parameters that can be calibrated, namely κ^*, λ^*, ν and c.

All the model parameters were directly obtained from the experimental data presented in the previous section, except for the Poisson's ratio and the rate of evolution of the anisotropy, which were determined using the above-outlined procedure. In the simulation of the tests with the JMC model, a unique set of calibrated parameters reported in Table 3 could be used for all samples of the different groups. The corresponding calibrated parameters for the SANICLAY model are listed in Table 4. For the slope of the compression line and unloading–reloading line, a different strategy was preferred, and specific values were calibrated on each sample group to account for their strong dependence on the organic content reported in Figure 5. The ratio κ^*/λ^* was fixed to 1/9. The adopted λ^* values are reported in Table 5.

4.2 | Stress State Initialisation

Three state variables are needed to initialise the proposed model, namely, the initial void ratio, e_i; corresponding to the initial mean

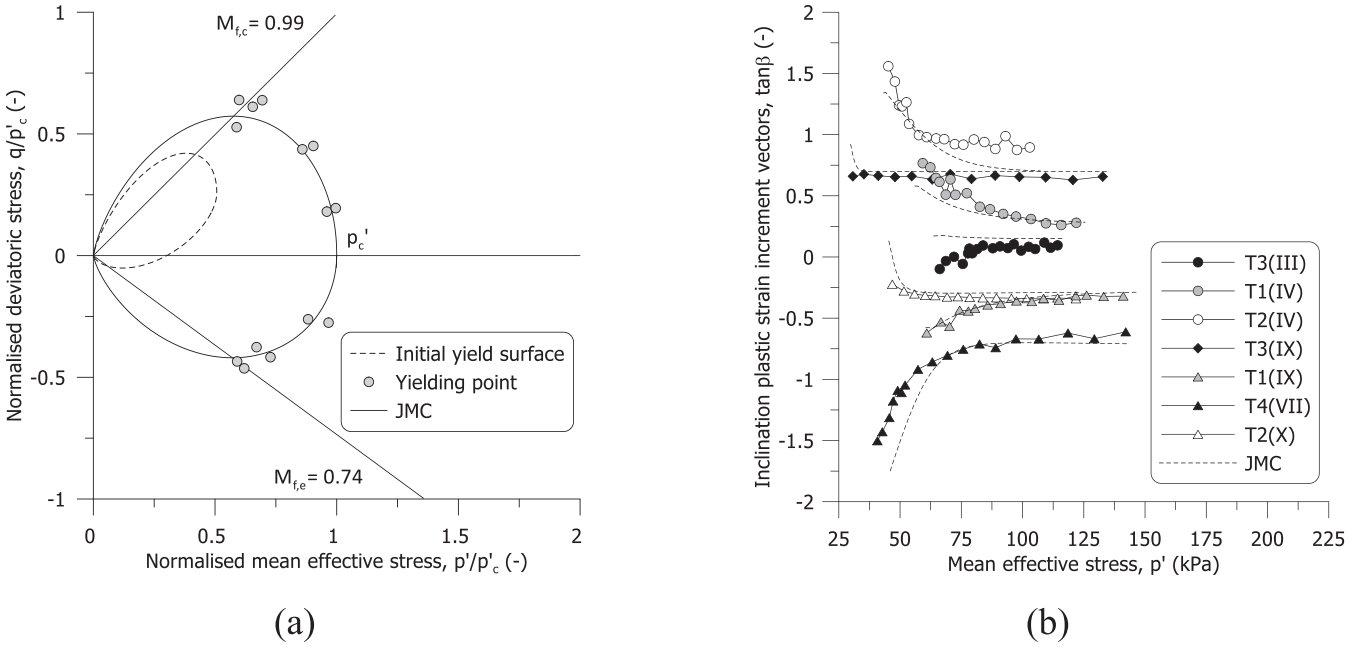

FIGURE 14 | Experimental data and numerical prediction for: (a) expanded and rotated yield locus after the first isotropic loading–unloading stage and (b) rotation of the plastic strain increment vectors along radial paths.

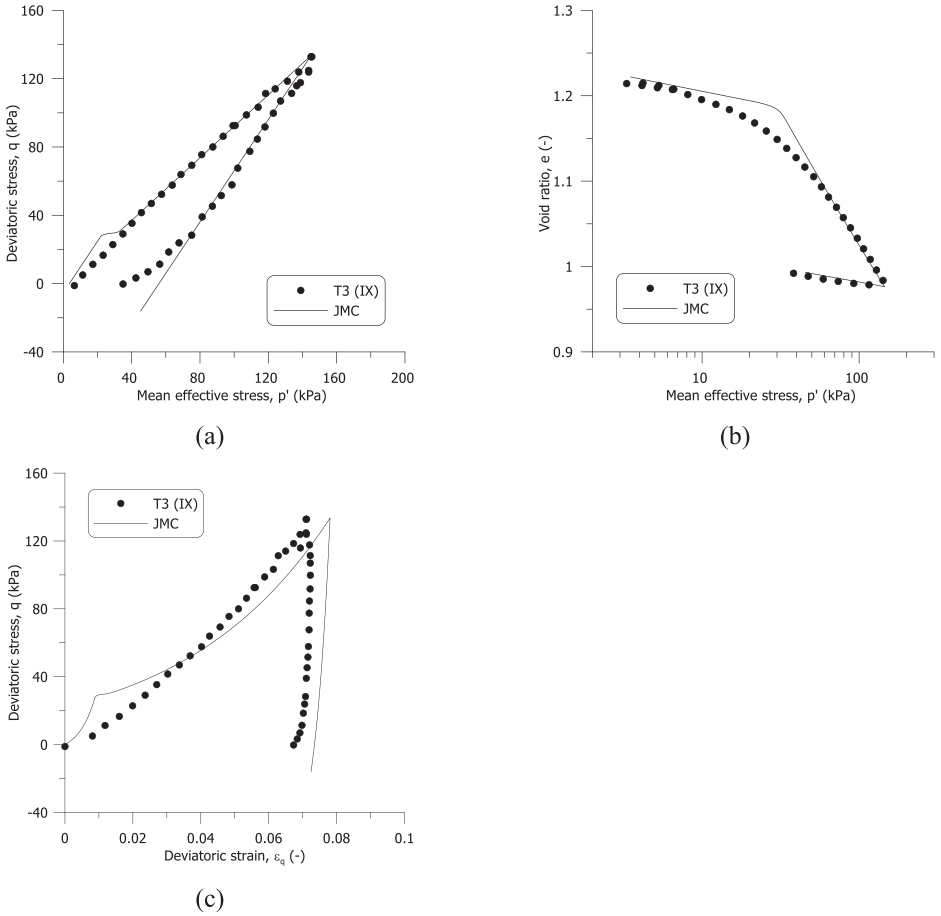

FIGURE 15 | Comparison between numerical simulations and experimental data for K_0 loading–unloading on sample T3 (IX).

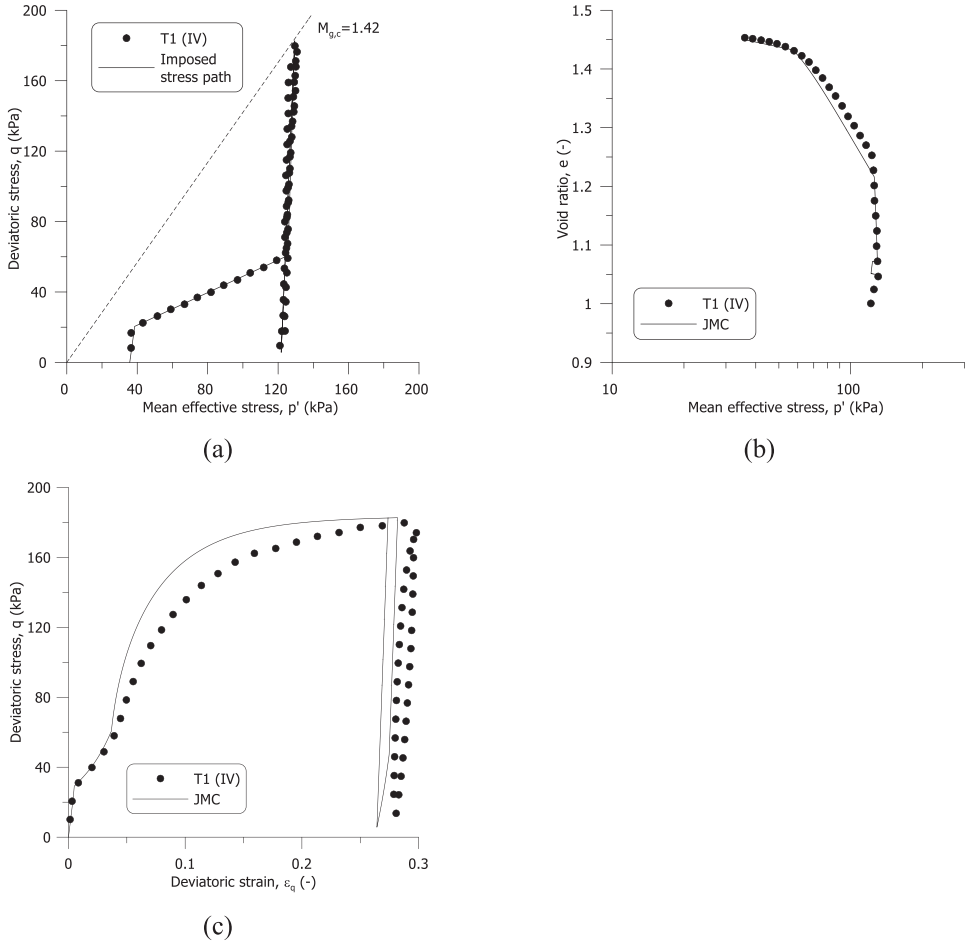

FIGURE 16 | Comparison between numerical simulations and experimental data for multiple drained stress paths including p' constant, radial path and p' constant loading–unloading path on sample T1 (IV).

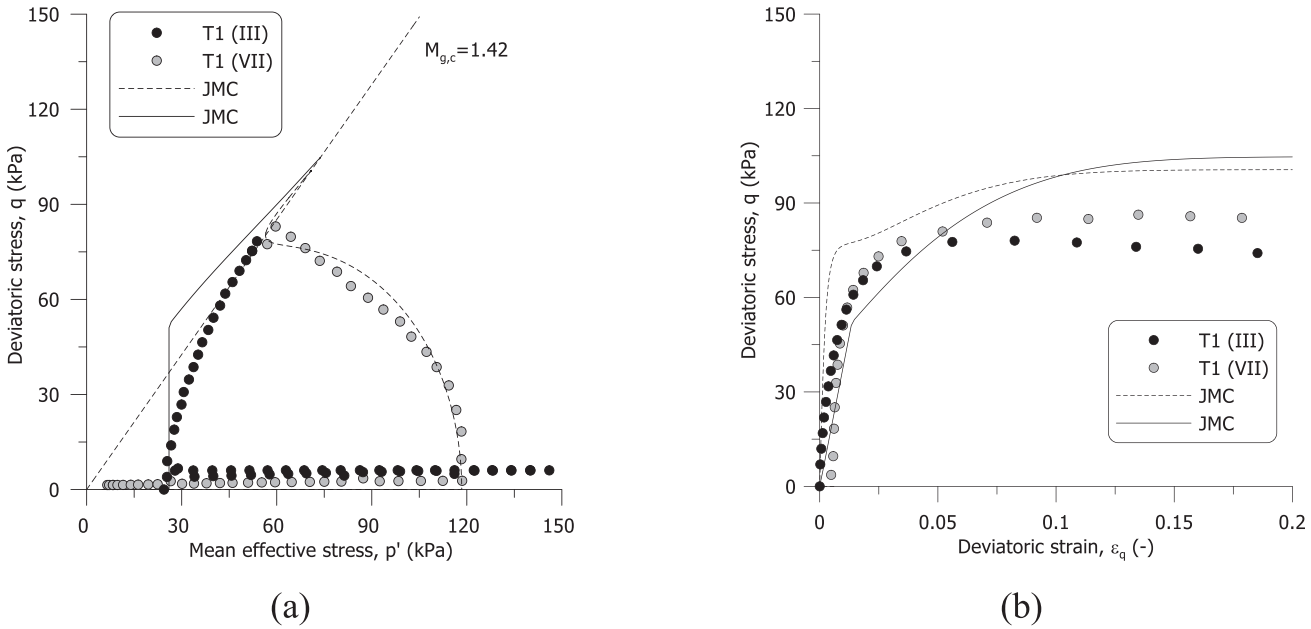

FIGURE 17 | Comparison between numerical simulations and experimental data for TxCIU tests on samples T1 (III) and T1 (VII).

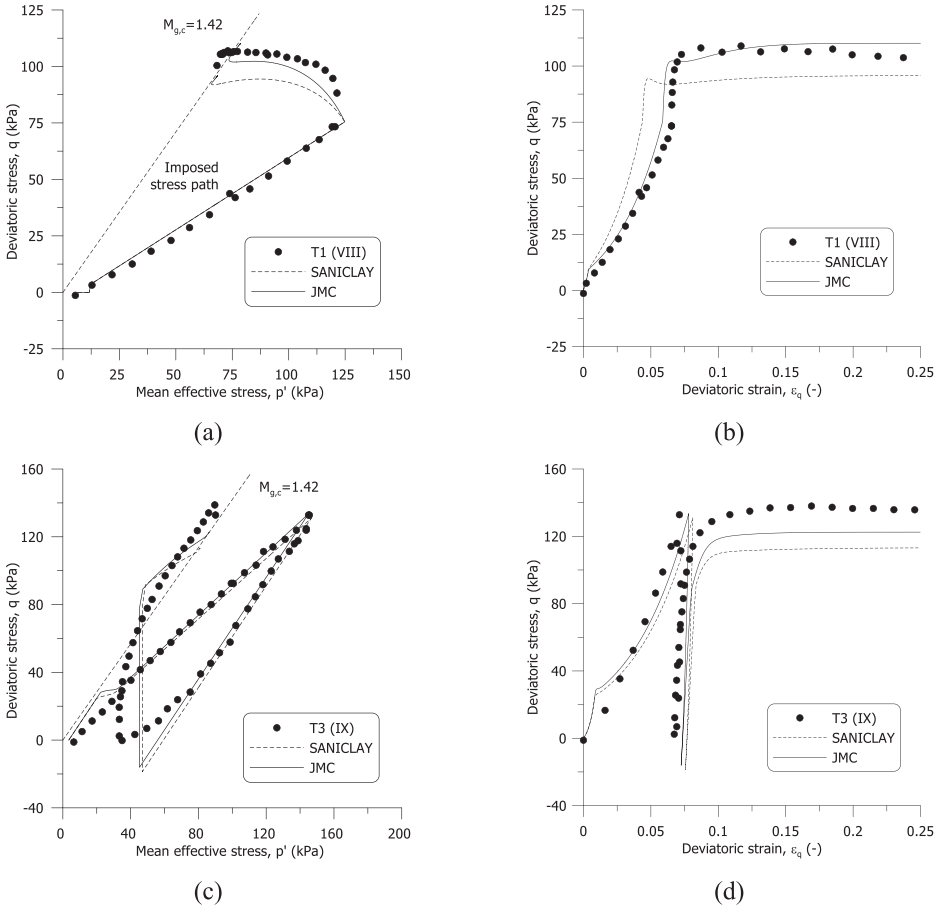

FIGURE 18 | Comparison between numerical simulations and experimental data for anisotropic TxCAU tests on samples T1 (VIII) and T3 (IX).

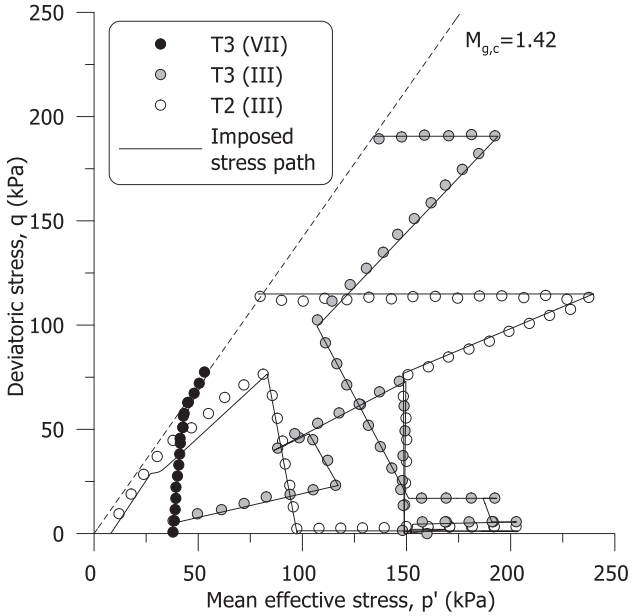

FIGURE 19 | Multistage drained triaxial compression tests used to validate the proposed model.

effective stress at the beginning of the triaxial test, p'_i; the initial pre-consolidation pressure, $p'_{c,i}$ and the initial inclination of the yield locus and plastic potential, α_i. The latter was determined assuming K_0 conditions when the sample was retrieved from the field. This assumption is discussed in the last section of the paper, that is, Section 5. The initial inclination is calculated as

$$\alpha_i = \frac{B\varepsilon\eta_{K_0}^3 + \eta_{K_0}^2 + \left[2\left(1-\kappa^*/\lambda^*\right) - BM_{g,c}^2\right]\varepsilon\eta_{K_0} - M_{g,c}^2}{2\varepsilon\left(1-\kappa^*/\lambda^*\right)} \quad ; \quad B = -\frac{2(1+\nu)}{9(1-2\nu)}\frac{\kappa^*}{\lambda^*} \tag{11}$$

where $\varepsilon = 3/2$ and η_{K_0} is the stress ratio corresponding to $K_0^{NC} = 0.43$ coming from Jaky's relationship. For normally consolidated conditions, the corresponding initial pre-consolidation pressure, $p'_{c,i}$, can be computed from Equation (2) with α_i and the estimated stress state in the field ($p'_{i,f}$, $q_{i,f}$).

$$p'_{i,f} = \frac{\sigma'_{v,i}\left(1+2K_0^{NC}\right)}{3} \qquad q_{i,f} = \sigma'_{v,i}\left(1-K_0^{NC}\right) \tag{12}$$

For overconsolidated conditions, the yield surface is initialised based on the estimated overconsolidation ratio.

4.3 | Evolution of the Yield Surface and Plastic Potential

The two new ingredients introduced in the JMC model from the experimental evidence are the flexible shape of the yield locus (Equation 2) and the asymptotic relationship for α_{gb} (Equation 8). To validate these choices, the model predictions for the yield

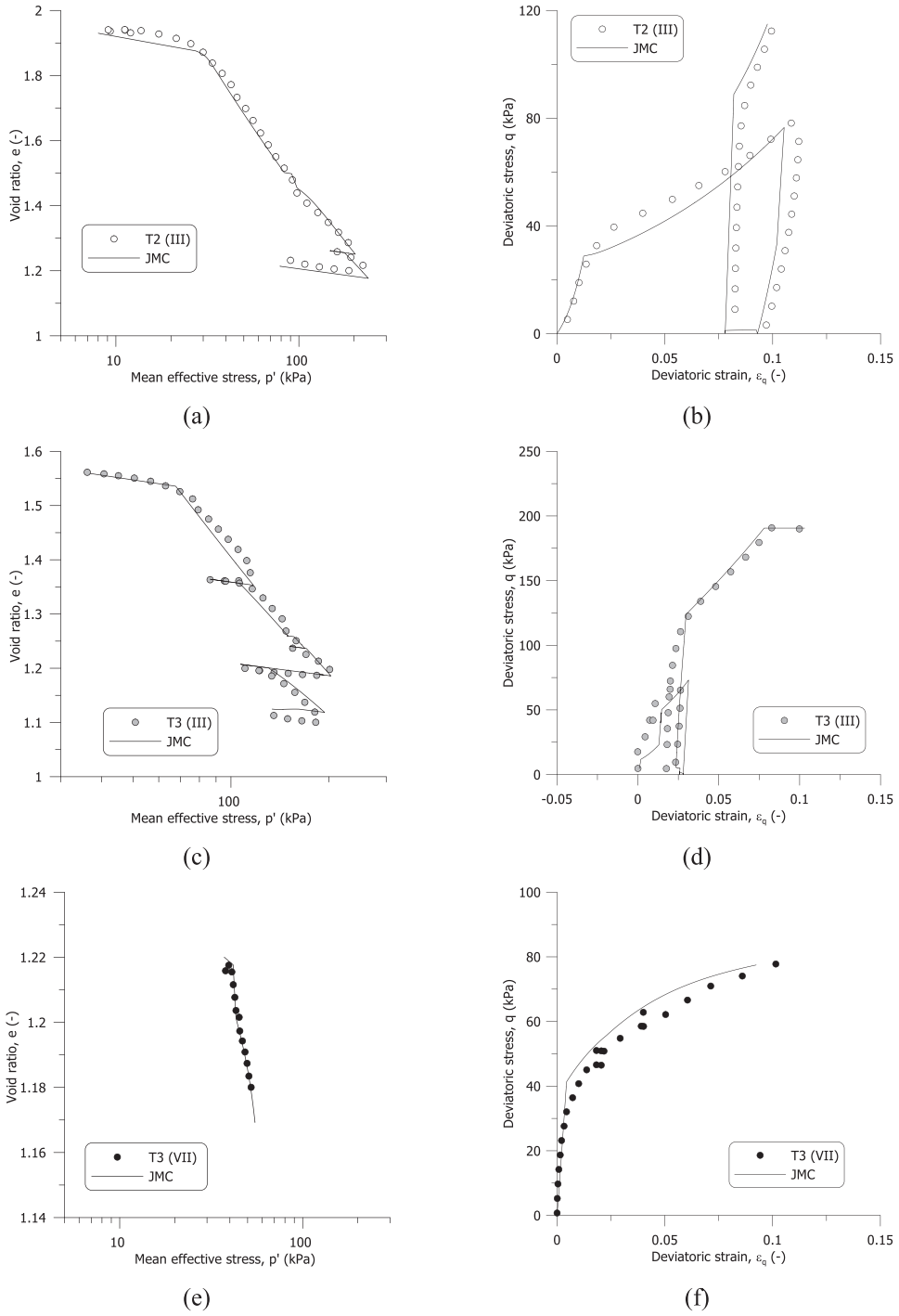

FIGURE 20 | Comparison between numerical simulations and experimental data from multistage drained triaxial compression tests on samples T2 (III), T3 (III) and T3 (VII).

locus and the evolution of the plastic strain increment vectors are analysed. Figure 14a displays the initial yield surface (dashed line) and the subsequent yield locus, expanded and rotated, predicted by the JMC after isotropic compression up to 70 kPa. The predicted yield surface fits very well with experimental yield points obtained on samples (T3 (III), T1 (IV), T2 (IV), T3–T4 (VII), T1–T2 (IX)) after isotropic loading up to 70 kPa, unloading to 40 kPa and shearing following different probing stress paths. Also, the model demonstrates excellent capability in describing the evolution of the plastic deformation mechanism both in compression and extension, as shown in Figure 14b, where the experimental and predicted rotation of the plastic strain increment vectors along radial paths are compared.

4.4 | Drained Triaxial Tests

The comparison between the experimental results and the model simulations is reported in Figure 15 for the K_0 loading–unloading test and in Figure 16 for a multiple drained stress

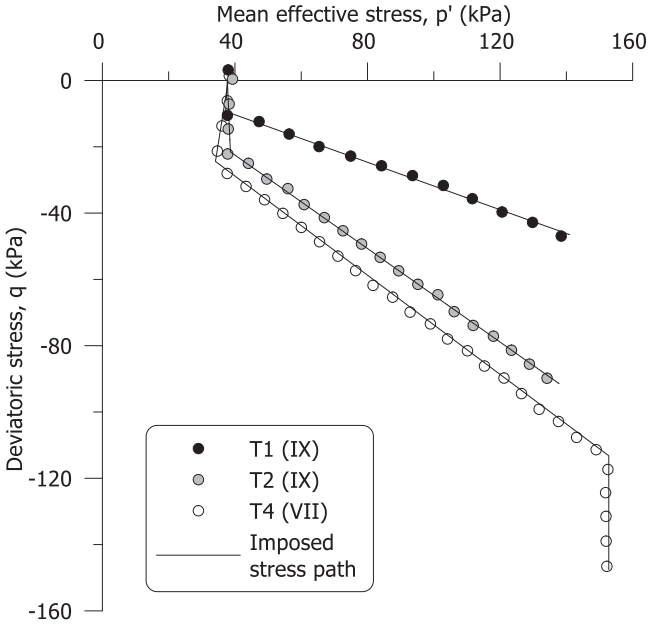

FIGURE 21 | Drained triaxial extension tests on samples slightly overconsolidated in the laboratory.

path, which includes p' constant, radial path and p' constant loading–unloading path.

The model correctly estimates the final stress path corresponding to the K_0^{NC} state given the calibration of the bounding values α_{gb}. At the beginning of the loading path, the model predicts higher overconsolidation than the one observed experimentally. Upon unloading, the predicted stress path follows reasonably well the experimental one until $p' = 80$ kPa, when the latter deviates, possibly indicating the occurrence of yielding. Both these observations seem to suggest that the shape of the yield locus on the dry side could be slightly narrower than the one adopted in Figure 10. Despite these small differences, the model simulation shows good qualitative and quantitative agreement with the experimental results, both in the volumetric and deviatoric response, for a wide range of strains. The qualitative and quantitative agreement between the JMC model and the experimental data is also confirmed by the multiple stress path in Figure 16.

4.5 | Undrained Triaxial Tests: TxCIU

Figure 17 shows the comparison between the experimental results and the numerical simulations of undrained triaxial compression tests on normally consolidated and overconsolidated (OCR = 6) samples, starting from isotropic conditions, T1 (III) and T1 (VII), respectively. For the normally consolidated side, the model shows good prediction of the initial stiffness and the overall stress path until the ultimate stress ratio, $M_{g,c} = 1.42$. After the attainment of $M_{g,c}$, the model shows a hook in the stress path with a further increase in the deviatoric stress, which is not observed in the experimental data. As already discussed by Dafalias and Taiebat [62], the discrepancy is a consequence of the absence of volumetric plastic strains in the rotation hardening rule (Equation 10). However, it is worth mentioning that geometrical effects in the triaxial setup may contribute to the sample ultimate deformation mechanism, as shown by Chao et al. [65].

The comparison with the overconsolidated sample T1 (III) highlights the limitations of the elastic–plastic model on the dry side, partially alleviated in the proposed formulation by adopting a rotational hardening and a yield locus with a smaller shape compared to the traditional modified Cam clay ellipse. The predicted stress path intercepts the yield locus for a stress ratio above the critical state before approaching asymptotically the critical state, while the experimental data show a smoother stress path reaching a lower ultimate deviatoric stress.

4.6 | Undrained Triaxial Tests: TxCAU

To better explore the predictive capabilities of the proposed model, Figure 18 shows the comparison between numerical simulations and anisotropically consolidated undrained compression tests, which better replicate stress–strain states relevant for field applications. With reference to the normally consolidated sample, T1 (VIII), the model shows very good agreement with the experimental data both in the pre-failure and failure state. Better performance compared to the original SANICLAY is due to the adopted shape of the yield locus, which helps in reproducing the observed stress path more accurately (Figure 18a). An equally good performance is found for the overconsolidated sample, T3 (IX), except for a slight underestimation of the deviatoric stress at failure, mainly due to the predicted elastic response over K_0 unloading (Figure 18c), as discussed previously.

4.7 | Multistage Drained Triaxial Compression Tests

Additional insight into the predictive capabilities of the model is shown on multistage drained compression tests, which included loading and unloading along a variety of stress path directions as displayed in Figure 19.

The comparison in Figure 20 shows very good performance of the JMC model on both the volumetric and deviatoric stress–strain response for a wide range of strains up to $\varepsilon_p \cong 0.3$ and $\varepsilon_q \cong 0.15$. It is worth remarking that the data in Figure 19 were only partially used (i.e., radial paths) to calibrate the bounding value α_{gb}, while all the other paths (e.g., unloading, reloading and shearing at constant q) are used to assess the model predictive capabilities. In spite of the simplicity of the elastic–plastic framework, the proposed model appears to be able to describe accurately the pre-failure behaviour of the tested material over non-conventional loading–unloading–reloading stress paths, which is particularly relevant for field assessment and monitoring.

4.8 | Drained Triaxial Extension Tests: Slightly Overconsolidated Samples

The model capabilities are evaluated in comparison with drained triaxial extension tests, which include an initial p' constant path followed by a radial path along different stress ratios (Figure 21).

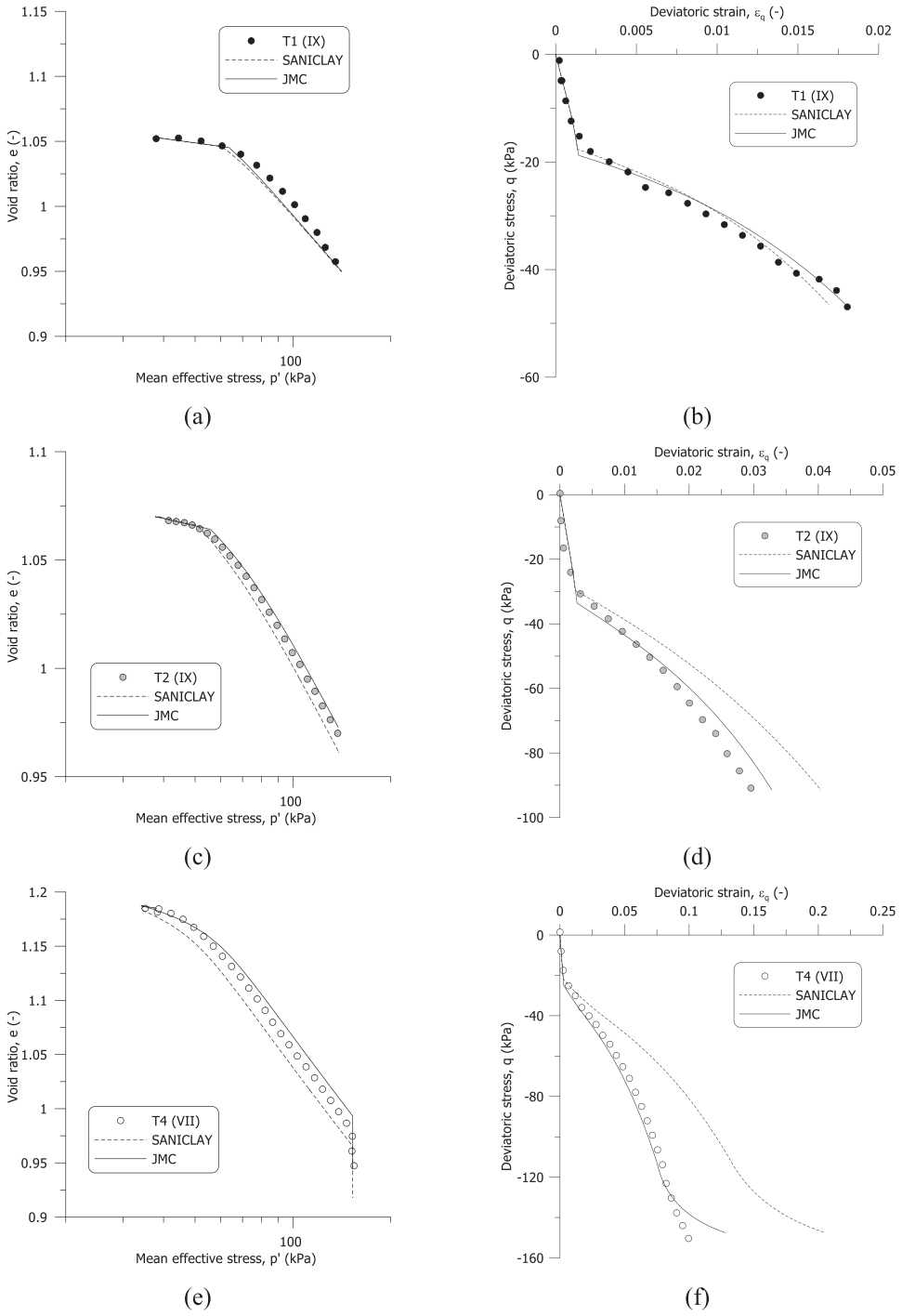

FIGURE 22 | Comparison between numerical simulations and experimental data from drained triaxial extension tests on samples T1 (IX), T2 (IX) and T4 (VII).

The samples were first isotropically loaded to $p'_c = 70$ kPa before unloading to $p'_s = 38$ kPa, corresponding to an OCR = 1.8 (Table 2).

The comparison in Figure 22 shows very good performance of the model on both the volumetric and deviatoric responses along the stress paths. The radial paths in Figure 21 were used to fix the asymptotic bounding values α_{gb} on the extension side (Figure 12). It is worth noticing that the model performs well in the entire pre-failure domain, showing a remarkable improvement compared to previous models, which is relevant in view of practical applications.

4.9 | Drained Triaxial Extension Tests Overconsolidated Samples From the Field

To better assess the advantages of the model over extension stress paths, the model predictive capabilities are evaluated with extension tests in Figure 23, performed on undisturbed samples

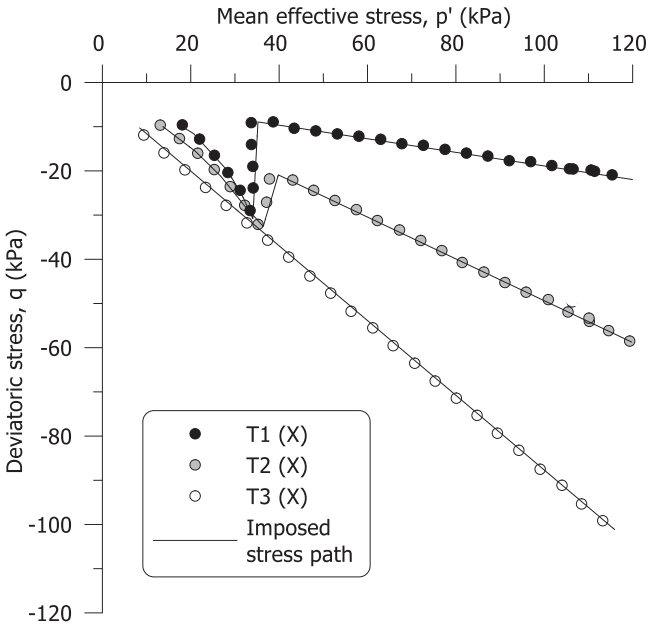

FIGURE 23 | Drained triaxial extension tests on overconsolidated samples in the field retrieved from the polder side.

from the polder side. Differently from the samples in Figure 21, these samples were sheared directly starting from the undisturbed state, with an estimated overconsolidation ratio OCR = 3 [39].

Both the JMC and the SANICLAY models show very good quantitative agreement on the volumetric response with the experimental data (Figure 24a,c,e). On the contrary, the quantitative agreement on the deviatoric stress–strain response is less satisfactory (Figure 24b,d,f). Both models overestimate the deviatoric strain, although the prediction of the new model is improving the one by SANICLAY, thanks to the extension of the formulation of the rotational hardening rule.

5 | Model Initialisation

Despite validation of the JMC model on the new dataset of experimental data, the model predictions in Figure 24 show a systematic overestimation of the deviatoric strain along the extension radial paths performed on undisturbed samples from the field. It should be noted that the model predictions depend not only on the model calibration but also on the model initialisation. For anisotropic models with rotational hardening, the OCR alone does not uniquely describe the previous stress history. Uncertainty in the full stress path experienced by the soil in the field can affect the predictions of the model for a given set of calibrated parameters. To exemplify the consequence of this uncertainty, the results of two different model initialisations, each coming from a plausible hypothesis on the field history, are discussed in the following.

The samples from group X (Figure 24) were retrieved from the polder side with an estimated in situ vertical effective stress σ_v' of about 15 kPa and estimated OCR = 3. In the previous simulations displayed in Figure 24, the initialisation of the hardening variables, $p'_{c,i}$ and α_i, followed the assumption of an overconsolidation state caused by 1-D loading/unloading, with a corresponding stress path and initial yield locus as depicted in Figure 25a. However, Ponzoni [41] had observed that the samples retrieved on the polder side were not fully saturated, with an estimated degree of saturation between 0.8 and 0.9. Given the water retention properties of the material, also reported by Ponzoni [41], this would correspond to a suction stress of about 35 kPa.

Based on this observation, a different initialisation of the yield surface from a standard K_0 mechanical loading/unloading was simulated, described by the stress path history depicted in Figure 25b. The equivalent isotropic suction stress was applied starting from a normally consolidated K_0 state, which overconsolidated the sample and, at the same time, contributed to re-orienting the inclination of the yield locus towards the p'-axis [66].

The stress paths imposed in the laboratory on samples from group (X) were simulated twice, each time starting from different initial yield surfaces. Figure 26 shows the influence of the two different initialisations on the computed deviatoric stress–strain response. The numerical results of sample T1 (X) considering a suction-induced overconsolidation state improved to a large extent and the stress–strain response very well matches the experimental data (Figure 26a). For test T2 (X) in Figure 26b, the model prediction still shows small overestimation of the deviatoric strain caused by the proximity of the stress ratio to the critical of one in extension, $M_{g,e}$, which reduces the shear stiffness to a greater extent than what is observed experimentally.

It must be observed that these results should not be considered as proof that drying was the origin of the OCR. Rather, they are included in the discussion to highlight to what extent constitutive models built on anisotropic yield surfaces require a robust initialisation strategy to support their reliable use in practical applications.

6 | Conclusions

Reliability of geotechnical design and assessment stems from advanced constitutive models, capable of modelling both the pre-failure and failure response of soils. In this work, a typical Dutch soft organic clay was investigated, to provide as thorough as possible insight on its stress–strain response over a variety of triaxial stress paths including extension ones, for which data are still scarce. The results were scrutinised to identify and tune relevant ingredients of an elastic–plastic modelling approach to be used in the practice.

The experimental programme was designed to elucidate compressibility and shear response, anisotropy and hardening of the organic clay. The experimental data show that the compressibility of the material may vary more than other features, depending on the organic content and the presence of diatoms. Over shear, the material displays a friction angle dependent on the Lode angle, based on triaxial compression and extension results. As expected, the depositional fabric is anisotropic and evolves rather quickly depending on the stress path. Careful analysis of drained probes results demonstrates that expansion of the

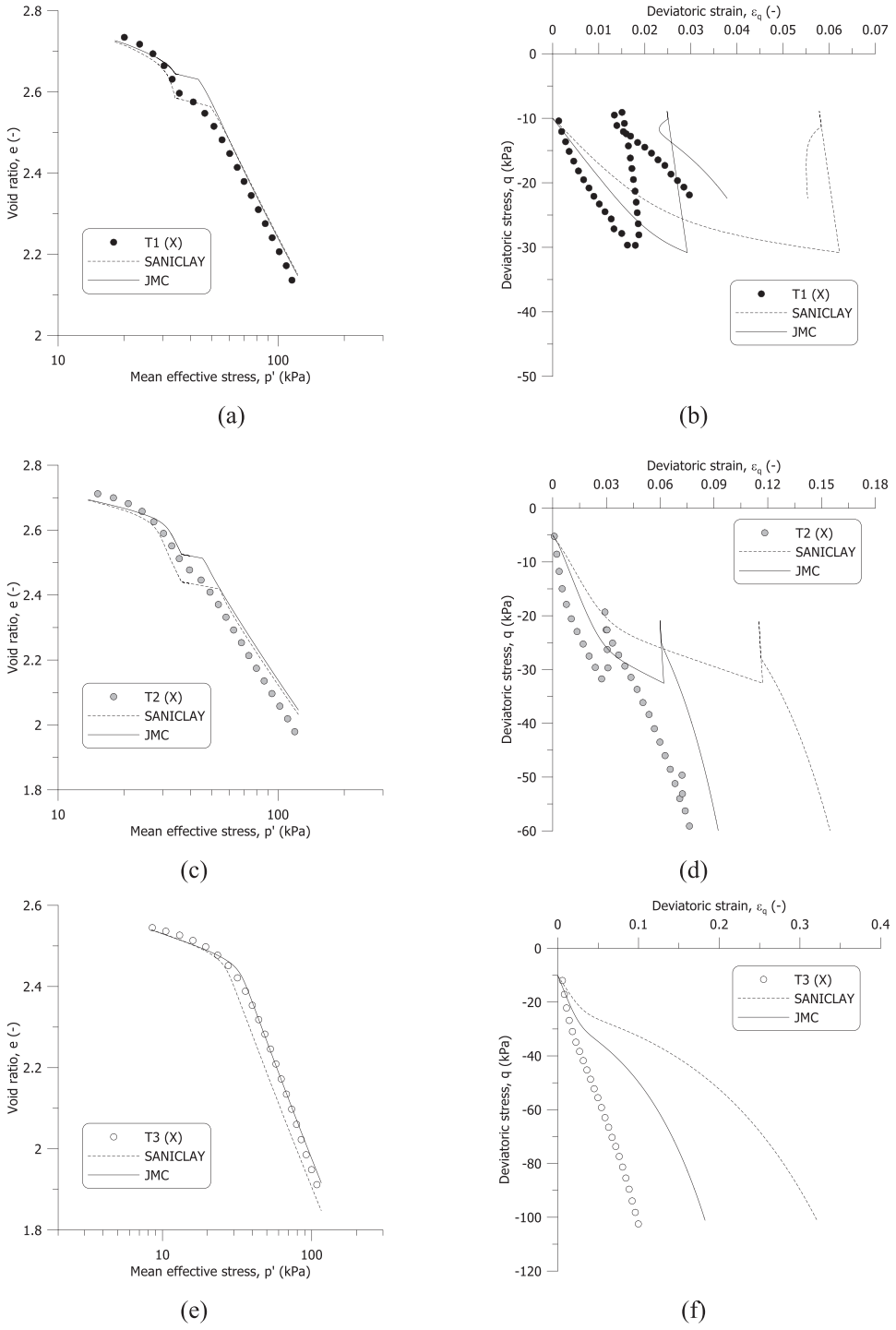

FIGURE 24 | Comparison between numerical simulations and experimental data from drained triaxial extension tests on samples T1 (X), T2 (X) and T3 (X).

yield locus is solely ruled by volumetric plastic strains, while the evolution of anisotropy depends on the loading direction.

Based on the previous experimental findings, a new constitutive model, JMC-clay is proposed. The model is built on the SANICLAY framework, which includes a non-associated flow rule, which was confirmed by the experimental results. The proposal extends the previous formulation, essentially by allowing flexibility to the yield surface shape and improving the rotational hardening rule with a dependence on the Lode angle. The benefits of JMC-clay can be appreciated especially in the deviatoric stress–strain response, and they become more and more evident at increasing stress ratio in extension. The proposed model should be sufficiently versatile for clays which do not suffer from significant destructuration.

The numerical simulations show that the proposed model can capture well the pre-failure response over non-monotonic loading

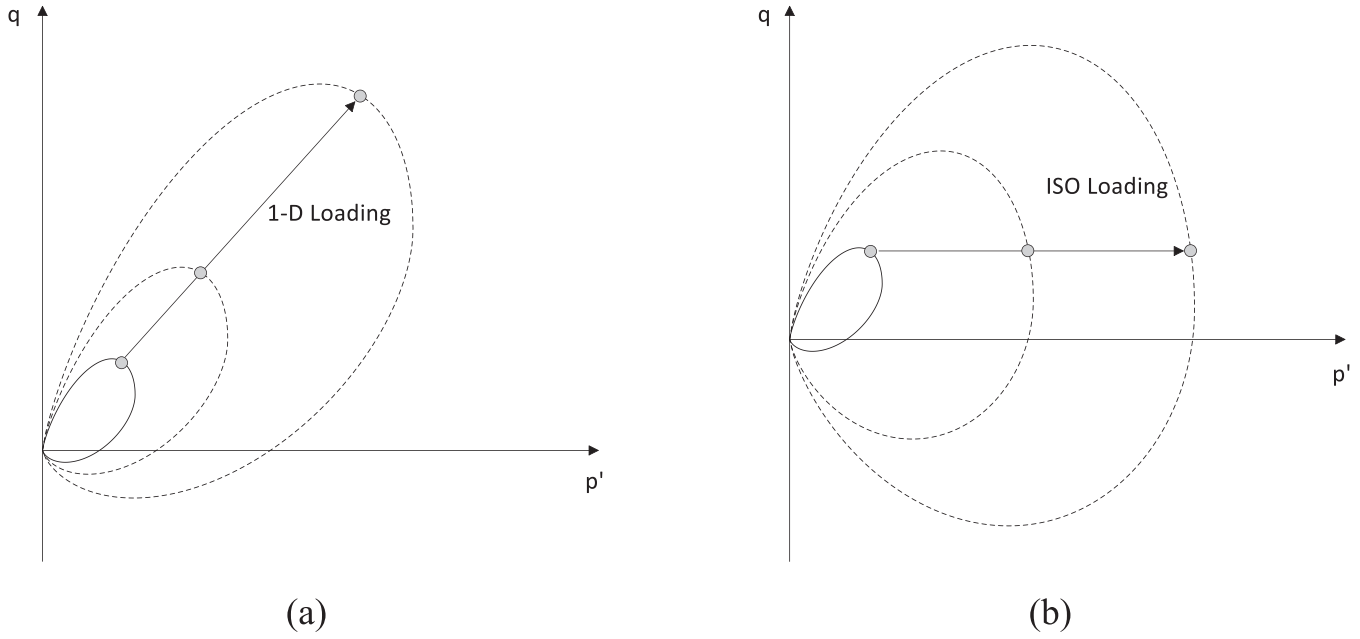

FIGURE 25 | Evolution of yield locus under (a) 1-D loading (b) isotropic loading for initialisation of the stress state.

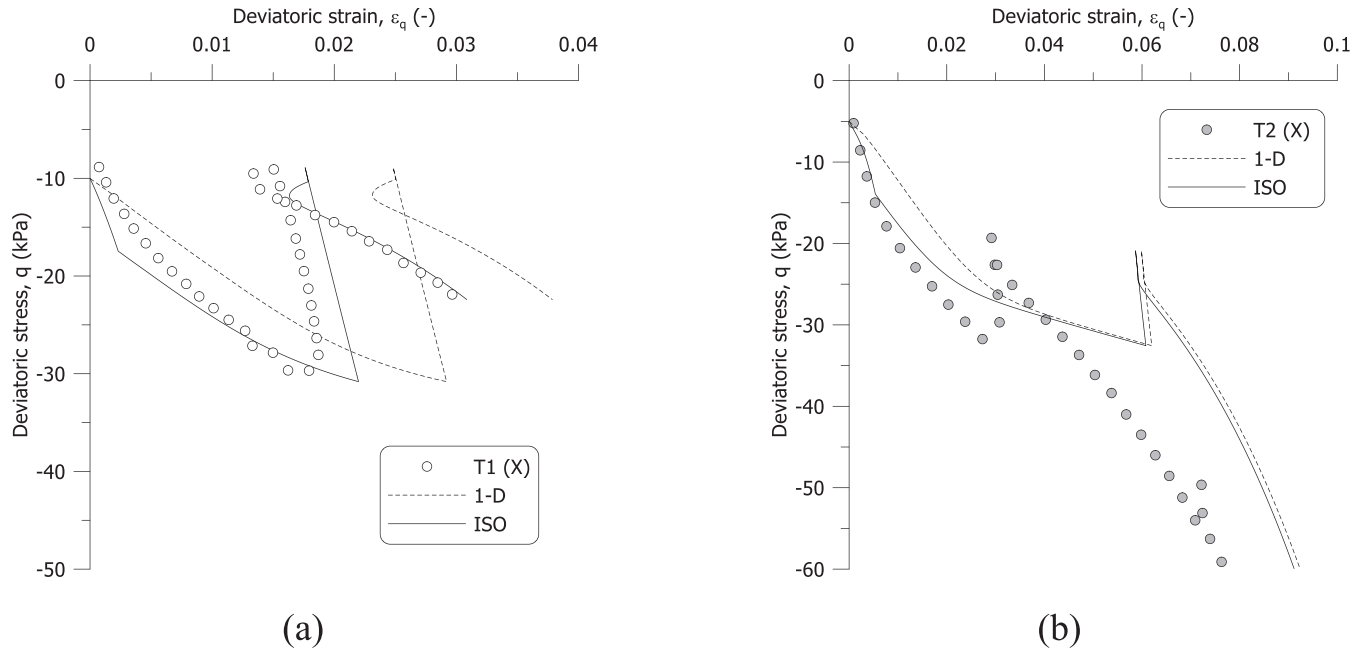

FIGURE 26 | Comparison between numerical simulations with two different model initialisation and experimental data: (a) T1 (X) and (b) T2 (X).

and unloading stress paths, which is a crucial feature for its implementation in the engineering practice. However, inspection of the limitations in the practical use reveals a strong dependence of the predicted response on the initialisation of the yield surface inclination, especially at low stresses. The latter observation suggests that the bottleneck in the practical use of this class of models lies more in the initialisation of the current state rather than in calibration, which can follow a rather simple strategy in the laboratory.

List of Symbols

d	dilatancy
e_0	initial void ratio
G	shear modulus
Gs	specific gravity
I_p	plasticity index
I_v	void index

K	bulk modulus
K_1	lateral stress ratio
K_0	at-rest lateral earth pressure coefficient
K_0^{NC}	at-rest lateral earth pressure coefficient in normally consolidated conditions
K_0^{OC}	at-rest lateral earth pressure coefficient in over-consolidated conditions
L	plastic multiplier
m	coefficient linking K_0^{NC}, K_0^{OC} and OCR
$M_{g,c}$	ultimate stress ratio in triaxial compression
$M_{g,e}$	ultimate stress ratio in triaxial extension
$M_{f,c}$, $M_{f,e}$, k_f	shape coefficients for the yield locus
OC	organic content
OCR	overconsolidation ratio
q	deviatoric stress
υ	specific volume
w	water content
w_p	plastic limit
w_l	liquid limit
z_c, z_e, s, y, c	coefficients of the rotational hardening rule
σ'_a	axial effective stress
σ'_r	radial effective stress
σ'_v	vertical effective stress
p'	mean effective stress
$p'_{c,max}$	maximum mean effective stress
p'_i	mean effective stress at the beginning of the triaxial test
p'_s	mean effective stress at the start of the shear
p'_c	pre-consolidation pressure
$p'_{c,n}$	normalised pre-consolidation pressure
η	stress ratio
ε_p	volumetric strain
ε_p^p	volumetric plastic strain
ε_q	deviatoric strain
λ_{1D-VCL}	slope of the 1D virgin normal compression line
$\lambda_{ISO-NCL}$	slope of the isotropic normal compression line
λ	slope of the normal compression line
κ	slope of the unloading–reloading line
κ^*	slope of the unloading–reloading line on the $\ln(\upsilon) - \ln(p')$ space
λ^*	slope of the normal compression line on the $\ln(\upsilon) - \ln(p')$ space
θ	Lode angle
φ'_c	ultimate friction angle in triaxial compression
φ'_e	ultimate friction angle in triaxial extension
$\delta\varepsilon_p^p$	volumetric plastic strain increment
$\delta\varepsilon_q^p$	deviatoric plastic strain increment
$\delta\varepsilon_p^e$	volumetric elastic strain increment
$\delta\varepsilon_q^e$	deviatoric elastic strain increment
$\delta p'$	mean effective stress increment
δq	deviatoric stress increment
$\delta p'_c$	pre-consolidation pressure increment
ν	Poisson's ratio
β	inclination of the plastic strain increment vector
p'_g	dummy variable for the plastic potential
α	rotational hardening variable
α_b	bounding value of the rotational hardening variable
α_f	rotational hardening variable of the yield locus
α_g	rotational hardening variable of the plastic potential
α_{gb}	bounding value of the rotational hardening variable of the plastic potential
$\delta\alpha$	increment of the rotational hardening variable
$\delta\alpha_f$	increment of the rotational hardening variable of the yield locus
$\delta\alpha_g$	increment of the rotational hardening variable of the plastic potential
p_{atm}	atmospheric pressure
α_i	initial inclination of the yield locus and plastic potential
$p'_{i,f}$	estimated mean effective stress in the field
$q_{i,f}$	estimated deviatoric stress in the field
$\sigma'_{v,i}$	estimated vertical effective stress in the field

Acknowledgements

The financial support of the Dutch Organisation for Scientific Research (NWO), under the project 'SOFTTOP: Investigating heterogeneous soft top soils for wave propagation, cyclic degradation and liquefaction potential' with project number DEEP.NL.2018.006 is gratefully acknowledged.

Conflicts of Interest

The authors declare no conflicts of interest.

Data Availability Statement

The data generated during or analysed during the current study are available from the corresponding author upon request.

References

1. R. Parry and V. Nadarajah, "Anisotropy in a Natural Soft Clayey Silt," *Engineering Geology* 8, no. 3 (1974): 287–309.

2. J. B. Burland, "On the Compressibility and Shear Strength of Natural Clays," *Géotechnique* 40, no. 3 (1990): 329–378.

3. D. Hight, A. Bond, and J. Legge, "Characterization of the Bothkennaar Clay: An Overview," *Géotechnique* 42, no. 2 (1992): 303–347.

4. L. Callisto and G. Calabresi, "Mechanical Behaviour of a Natural Soft Clay," *Géotechnique* 48, no. 4 (1998): 495–513.

5. L. Zdravković, D. Potts, and D. Hight, "The Effect of Strength Anisotropy on the Behaviour of Embankments on Soft Ground," *Géotechnique* 52, no. 6 (2002): 447–457.

6. J. Pineda, L. Suwal, R. Kelly, L. Bates, and S. Sloan, "Characterisation of Ballina Clay," *Géotechnique* 66, no. 7 (2016): 556–577.

7. L. Bjerrum, "Engineering Geology of Norwegian Normally-Consolidated Marine Clays as Related to Settlements of Buildings," *Geotechnique* 17, no. 2 (1967): 83–118.

8. J. Graham, J. Crooks, and A. L. Bell, "Time Effects on the Stress-Strain Behaviour of Natural Soft Clays," *Géotechnique* 33, no. 3 (1983): 327–340.

9. T. C. Sheahan, C. C. Ladd, and J. T. Germaine, "Rate-Dependent Undrained Shear Behavior of Saturated Clay," *Journal of Geotechnical Engineering* 122, no. 2 (1996): 99–108.

10. M. Karstunen, H. Krenn, S. J. Wheeler, M. Koskinen, and R. Zentar, "Effect of Anisotropy and Destructuration on the Behavior of Murro Test Embankment," *International Journal of Geomechanics* 5, no. 2 (2005): 87–97.

11. D. Mašín, "A Hypoplastic Constitutive Model for Clays," *International Journal for Numerical and Analytical Methods in Geomechanics* 29, no. 4 (2005): 311–336.

12. G. Seidalinov and M. Taiebat, "Bounding Surface SANICLAY Plasticity Model for Cyclic Clay Behavior," *International Journal for Numerical and Analytical Methods in Geomechanics* 38, no. 7 (2014): 702–724.

13. M. Rezania, H. Nguyen, H. Zanganeh, and M. Taiebat, "Numerical Analysis of Ballina Test Embankment on a Soft Structured Clay Foundation," *Computers and Geotechnics* 93 (2018): 61–74.

14. M. Leoni, M. Karstunen, and P. Vermeer, "Anisotropic Creep Model for Soft Soils," *Géotechnique* 58, no. 3 (2008): 215–226.

15. N. Sivasithamparam, M. Karstunen, and P. Bonnier, "Modelling Creep Behaviour of Anisotropic Soft Soils," *Computers and Geotechnics* 69 (2015): 46–57.

16. M. Rezania, M. Taiebat, and E. Poletti, "A Viscoplastic SANICLAY Model for Natural Soft Soils," *Computers and Geotechnics* 73 (2016): 128–141.

17. B. Z. Coelho, J. Dijkstra, and M. Karstunen, "Viscoplastic Cyclic Degradation Model for Soft Natural Soils," *Computers Geotechnics* 135 (2021): 104176.

18. J. Jiang, H. I. Ling, and V. N. Kaliakin, "An Associative and Non-Associative Anisotropic Bounding Surface Model for Clay," *Journal of Applied Mechanics* 79, no. 3 (2012): 1010.

19. M. Rezania and H. Dejaloud, "BS-CLAY1: Anisotropic Bounding Surface Constitutive Model for Natural Clays," *Computers and Geotechnics* 135 (2021): 104099.

20. H. Sekiguchi and H. Ohta, "Induced Anisotropy and Time Dependancy in Clays," in 9th ICSMFE Tokyo (1977), 229–238.

21. K. Hashiguchi, "An Expression of Anisotropy in a Plastic Constitutive Equation of Soils," in 9th ICSMFE Tokyo (1977), 302–305.

22. S. J. Wheeler, A. Näätänen, M. Karstunen, and M. Lojander, "An Anisotropic Elastoplastic Model for Soft Clays," *Canadian Geotechnical Journal* 40, no. 2 (2003): 403–418.

23. F. Dafalias, M. T. Manzari, and A. G. Papadimitriou, "SANICLAY: Simple Anisotropic Clay Plasticity Model," *International Journal for Numerical and Analytical Methods in Geomechanics* 30, no. 12 (2006): 1231–1257.

24. K. H. Roscoe and J. Burland, On the Generalized Stress-Strain Behaviour of Wet Clay (1968).

25. M. Huang, Y. Liu, and D. Sheng, "Simulation of Yielding and Stress–Stain Behavior of Shanghai Soft Clay," *Computers and Geotechnics* 38, no. 3 (2011): 341–353.

26. M. Yamada, M. Akaishi, and Y. F. Dafalias, "Undrained Strain Softening Behavior of Normally Consolidated Clays and Mud Rocks," *Journal of Geotechnical Engineering JSCE* no. 687 (2001): 1–8.

27. J. Tigchelaar, J. W. de Feijter, and E. J. den Haan, "Shear Tests on Reconstituted Oostvaardersplassen Clay," in Soft Ground Technology (2001), 67–81.

28. E. Den Haan, "Sample Disturbance of Soft Organic Oostvaarder-splassen Clay," in *Deformation Characteristics of Geomaterials*, ed. Di Benedetto et al. (Balkema Publisher, 2003), 49–55.

29. X. Cheng, H. Janssen, and F. B. Barends, "A Combination of ESEM, EDX and XRD Studies on the Fabric of Dutch Organic Clay From Oostvaardersplassen (Netherlands) and Its Geotechnical Implications," *Applied Clay Science* 25, no. 3-4 (2004): 179–185.

30. X. Cheng, D. Ngan-Tillard, and E. Den Haan, "The Causes of the High Friction Angle of Dutch Organic Soils," *Engineering Geology* 93, no. 1-2 (2007): 31–44.

31. C. Jommi, D. Sterpi, T. de Gast, S. Muraro, E. Ponzoni, and H. van Hemert, "*Coupled Hydro-Mechanical Analysis of the Pre-Failure and the Failure Behaviour of a Dyke on Soft Subsoil: Formulation and Synthesis of Results*," in ICOLD International Benchmark Workshop on Numerical Analysis of Dams, ICOLD-BW (2019), 645–665.

32. K. H. Head, *Manual of Soil Laboratory Testing – Vol. I: Soil Classification and Compaction Tests* (Whitteles Publishing, 2014).

33. D5550-14 A, *Standard Test Method for Specific Gravity of Soil Solids by Gas Pycnometer* (American Society of Testing and Materials, 2014).

34. D2974-14 A, *Standard Test Methods for Moisture, Ash, and Organic Matter of Peat and Other Organic Soils* (American Society of Testing and Materials, 2014).

35. S. Muraro and C. Jommi, "Implication of End Restraint in Triaxial Tests on the Derivation of the Stress-Dilatancy Rule for Soils Having High Compressibility," *Canadian Geotechnical Journal* 56, no. 6 (2019): 840–851.

36. S. Muraro and C. Jommi, "Experimental Determination of Shear Strength of Peat From Standard Undrained Triaxial Tests: Correcting for the Effects of End Restraint," *Géotechnique* 71, no. 1 (2021): 76–87.

37. P. Ludwik, *Elemente der Technologischen Mechanik* (Springer-Verlag, 1909).

38. C. Jommi, C. Y. Chao, S. Muraro, and H. F. Zhao, "Developing a Constitutive Approach for Peats From Laboratory Data," *Geomechanics for Energy and the Environment* 27 (2021): 100220, https://doi.org/10.1016/j.gete.2020.100220.

39. A. Nocilla, M. R. Coop, and F. Colleselli, "The Mechanics of an Italian Silt: An Example of 'Transitional' Behaviour," *Géotechnique* 56, no. 4 (2006): 261–271.

40. E. Ponzoni, A. Nocilla, M. R. Coop, and F. Colleselli, "Identification and Quantification of Transitional Modes of Behaviour in Sediments of Venice Lagoon," *Géotechnique* 64, no. 9 (2014): 694–708.

41. E. Ponzoni, "Historical Constructions on Natural Silty Soils Accounting for the Interaction With the Atmosphere," (PhD thesis, Università degli studi di Brescia, 2017).

42. B. Caicedo, C. Mendoza, F. López, and A. Lizcano, "Behavior of Diatomaceous Soil in Lacustrine Deposits of Bogotá, Colombia," *Journal of Rock Mechanics Geotechnical Engineering* 10, no. 2 (2018): 367–379.

43. R. C. Leal Reina, *Influencia del Contenido de Materia Orgánica en el Cambio Volumétrico de Arcillas Blandas* (Universidad Nacional de Colombia, 2019).

44. K. Y. Lo, "Shear Strength Properties of a Sample of Volcanic Material of the Valley of Mexico," *Geotechnique* 12, no. 4 (1962): 303–318.

45. G. Mesri, A. Rokhsar, and B. F. Bohor, "Composition and Compressibility of Typical Samples of Mexico City Clay," *Geotechnique* 25, no. 3 (1975): 527–554.

46. H. Tanaka and J. Locat, "A Microstructural Investigation of Osaka Bay Clay: the Impact of Microfossils on Its Mechanical Behaviour," *Canadian Geotechnical Journal* 36, no. 3 (1999): 493–508.

47. J. A. Diaz-Rodriguez, S. Leroueil, and J. D. Aleman, "Yielding of Mexico City Clay and Other Natural Clays," *Journal of Geotechnical Engineering* 118, no. 7 (1992): 981–995.

48. D. R. Shiwakoti, H. Tanaka, M. Tanaka, and J. Locat, "Influences of Diatom Microfossils on Engineering Properties of Soils," *Soils and Foundations* 42, no. 3 (2002): 1–17.

49. X. Zhang, X. Liu, Y. Xu, G. Wang, and Y. J. Ren, "Compressibility, Permeability and Microstructure of Fine-Grained Soils Containing Diatom Microfossils," *Géotechnique* 74, no. 7 (2024): 661–675.

50. B. Schmidt, "Earth Pressures at Rest Related to Stress History," *Canadian Geotechnical Journal* 3, no. 4 (1966): 239–242.

51. P. W. Mayne and F. H. Kulhawy, "K-OCR Relationships in Soil," *Journal of the Geotechnical Engineering Division* 108, no. GT6 (1982): 851–872.

52. S. Leroueil and P. R. Vaughan, "The General and Congruent Effects of Structure in Natural Soils and Weak Rocks," *Géotechnique* 40, no. 3 (1990): 467–488.

53. Y. Watabe, M. Tanaka, H. Tanaka, and T. Tsuchida, "K0-Consolidation in a Triaxial Cell and Evaluation of In-Situ K0 for Marine Clays With Various Characteristics," *Soils and Foundations* 43, no. 1 (2003): 1–20.

54. F. Cotecchia and R. J. Chandler, "The Influence of Structure on the Pre-Failure Behaviour of a Natural Clay," *Géotechnique* 47, no. 3 (1997): 523–544.

55. D. E. Becker, J. H. A. Crooks, K. Been, and M. G. Jefferies, "Work as a Criterion for Determining In Situ and Yield Stresses in Clays," *Canadian Geotechnical Journal* 24, no. 4 (1987): 549–564.

56. D. M. Wood, *Soil Behaviour and Critical State Soil Mechanics* (Cambridge University Press, 1990).

57. S. Muraro and C. Jommi, "Pre-Failure Behaviour of Reconstituted Peats in Triaxial Compression," *Acta Geotechnica* 16 (2021): 789–805, https://doi.org/10.1007/s11440-020-01019-2.

58. G. R. McDowell and K. W. Hau, "A Simple Non-Associated Three Surface Kinematic Hardening Model," *Géotechnique* 53, no. 4 (2003): 433–437.

59. Y. F. Dafalias, "An Anisotropic Critical state Soil Plasticity Model," *Mechanics Research Communications* 13, no. 6 (1986): 341–347.

60. P. K. K. Wong and R. J. Mitchell, "Yielding and Plastic Flow of Sensitive Cemented Clay," *Geotechnique* 25, no. 4 (1975): 763–782.

61. T. A. Newson and M. C. R. Davies, "A Rotational Hardening Constitutive Model for Anisotropically Consolidated Clay," *Soils and Foundations* 36, no. 3 (1996): 13–20.

62. Y. F. Dafalias and M. Taiebat, "Anatomy of Rotational Hardening in Clay Plasticity," *Géotechnique* 63, no. 16 (2013): 1406–1418.

63. Z. Y. Yin and C. S. Chang, "Non-Uniqueness of Critical state Line in Compression and Extension Conditions," *International Journal for Numerical Analytical Methods in Geomechanics* 33, no. 10 (2009): 1315–1338.

64. J. Jiang and H. I. Ling, "A Framework of an Anisotropic Elastoplastic Model for Clays," *Journal of Mechanics Research Communications* 37, no. 4 (2010): 394–398.

65. C. Chao, S. Muraro, and C. Jommi, "Numerical Investigation of the Equipment Set-Up in Triaxial Testing of Soft Soils," In Proceedings 10th NUMGE (2023).

66. E. Romero and C. Jommi, "An Insight into the Role of Hydraulic History on the Volume Changes of Anisotropic Clayey Soils," *Water Resources Research* 44 (2008): W12412.